Forum for Electromagnetic Research Methods and Application Technologies (FERMAT)

Electromagnetic Field Shielding of a Spherical Shell – Revisited

Frederick M. Tesche
1519 Miller Mountain Road
Saluda, NC 28773
(Email: Fred@Tesche.com)

Abstract—**This paper takes a fresh look at two classical electromagnetic (EM) shielding problems involving 1) a time harmonic analysis of a closed, imperfectly conducting spherical shell and, 2) a quasi-static analysis of a perfectly conducting hollow sphere with an aperture. Previous studies of the EM shielding provided by these geometries have concentrated on evaluating the E- and H-fields at the center of the shield. While the internal H-field in the shielded volume of the conducting shell is very close to being constant, the same is not true for the E-field, where there can be a significant variation in the E-field intensity from point to point within the interior.**

For both of these canonical shielding problems, the analysis methods are reviewed and are used to determine cumulative probability distributions for the fields within the shielded volume.

In implementing the analysis for the conducting shell, the use of scaled Hankel functions is described. This is used to avoid numerical difficulties in evaluating the spherical harmonic solution for lossy medium. Additionally, closed-form expressions for the wave expansion coefficients in the spherical coordinate system are derived. The analysis of the hollow sphere with an aperture likewise permits the determination of the E-fields anywhere in and around the sphere.

Index Terms—**EM Shielding, Spherical Shield, Sphere with Aperture, Spherical Harmonic Expansions, Scaled Spherical Harmonics.**

I. INTRODUCTION

There is a continuing need to understand and describe the electromagnetic (EM) field environment inside a protective enclosure illuminated by an exterior source. There are several EM standards [1]–[3] that provide measurement procedures for obtaining shielding effectiveness parameters for enclosures and these standards are often used as requirements for the design and procurement of equipment protected against external EM fields.

Most of the standards recognize the fact that the EM field within a real enclosure will vary with position and polarization. Thus, the test procedures usually involve making several measurements of the internal field and determining a worst-case shielding estimate. However, due to time and budget constraints, it is unlikely that sufficient measurements are made to develop a robust statistical representation of the internal fields.

It is possible to use a computational model of an enclosure to determine the internal EM field and its spatial variability. Such models can involve simple canonical shapes like a conducting slab, a cavity bounded by two slabs, a cylinder or a sphere [4]-[5]. More complicated models of realistic enclosures having apertures and conducting penetrations are also possible using a finite-difference time domain (FDTD) procedure for solving Maxwell’s equations in and around the enclosure [6].

The simplest, yet somewhat realistic, model for shielding is a spherical enclosure. Unlike the infinite cylinder or one or more conducting slabs, the sphere has a finite volume, which is more typical of a realistic enclosure. Moreover, the EM field in the vicinity of the sphere can be described by relatively simple mathematical functions that permit a numerical computation of the shielding of external fields.

Using the spherical wave functions defined by Stratton [7], Harrison and Papas [8] have developed expressions for the E- and H-field at the center of a thin spherical shield due to an incident plane wave excitation. Lindell [9] has examined Harrison’s solution near the natural resonances of the sphere, and Shastry [10] has analyzed a hemisphere being excited by a point dipole source. Baum [11] has also examined this problem as a special case illustrating the use of the boundary connection supermatrix (BCS) of a sphere. While all of these investigators have used a modal expansion technique for the solution of the sphere shielding problem, Franschetti [12] has employed an integral equation approach. In each of these references, only the E-fields at the center of the sphere have been considered[1].

Real enclosures have openings, so perhaps a uniform spherical model is not the best one to use for understanding the behavior of the internal fields. References [13]-[15] have described analysis procedures for treating a spherical shell with a circular aperture. However, their emphasis is on the scattered EM field and not the internal field distribution. Sancer [16] has described a frequency dependent dual series solution for the internal field in a sphere with a hole, and has used this model to determine the quasi-static E and H-fields only at the center of the spherical cavity. Casey [17] has solved the same problem using a quasi-static dual series model for the E-field at the center of the sphere. A more general frequency dependent solution for the internal fields in a sphere has been described by Senior in [18]. This solution involves a modal expansion for the E-fields and is based on the earlier work of [13]. The applicability of this work is in the resonance region of the sphere.

---

[1] This may be due to two reasons. First, at the center only the $n = 1$ spherical harmonic is needed, so that evaluating an infinite series summation is not required. Second, it is well-known that the quasi-static magnetic field is constant within the sphere volume, and using the center as the B-field observation point is a good choice. Perhaps it was thought that this location would also be suitable for the E-field. However, as will be shown later, the E-field in the sphere varies significantly with position, and the E-field at the center is significantly lower than the average value of E within the sphere.

The work reported in this paper is a re-visitation of two classical canonical shielding problems: 1) a thin spherical shell made of imperfectly conducting, and possibly magnetic material, and 2) a perfectly conducting hollow sphere with an aperture. Section II describes the analysis of the penetrable sphere by using expansion of spherical vector wave functions in the three regions of the sphere: inside and outside the sphere and in the wall material. In performing this analysis, closed form expressions for the expansion coefficients are determined and a method for eliminating numerical overflow errors in evaluating various Hankel functions in the wave expansions is described. With a computer program developed to evaluate the E- and H-fields anywhere within the shielded volume of the shell, a Monte Carlo simulation has been performed to generate data suitable for describing the cumulative probability distributions (CPD) for the internal E and H fields.

In Section III, a quasi-static model useful for computing the internal E-field in a sphere with a hole is reviewed. Because the dual H-field problem can be solved from the E-field solution in this case (see [16]), only the E-field shielding is discussed here. A Monte Carlo simulation is also performed for this shield, and the corresponding CPDs for the E-field are presented.

Section IV concludes this paper with a review and comments. References are provided in Section V.

II. EM SHIELDING BY A SPHERICAL SHELL

In this section, the classical solution for shielding of a spherical shell of imperfectly conducting material is reviewed and the behavior of the internal and external E and H-fields is examined. This solution involves a spherical harmonic expansion of the fields with expansion coefficients determined from suitable boundary conditions on the sphere. This analysis is essentially the same as described by Harrison and Papas [8] and others. However, [8] only provides the expressions for the field expansion coefficients for the internal fields and it concentrates on the fields at the center of the sphere. In the development here, we will provide closed-form expressions for all field coefficients for all regions. In addition, in the present development we pay special attention to the machine computation of the spherical Hankel functions, which are needed in the solution for the fields. In particular, we describe a simple modification of the classical spherical wave expansion functions that permit an accurate evaluation of the E and H-fields inside and outside the shell.

A. Problem Geometry

The geometry of the spherical shell illuminated by an incident plane wave propagating in the z-direction is shown in Figure 1.

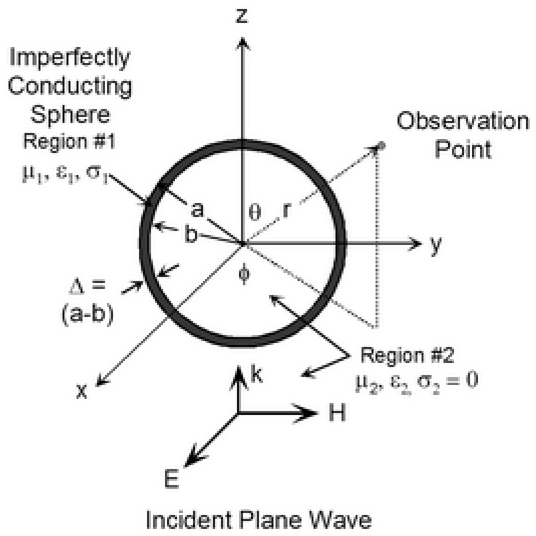
z
Imperfectly Conducting Sphere
Region #1
μ_1, ε_1, σ_1
a
b
θ
r
Observation Point
y
φ
Δ = (a-b)
x
k
H
E
Region #2
μ_2, ε_2, $\sigma_2 = 0$
Incident Plane Wave

Figure 1. Illustration of a spherical shell illuminated by an incident plane wave.

The incident E-field is in the *x*-direction, with the H-field in the *y*-direction. The spherical shell is designated as region #1, and has outer and inner radii of *a* and *b*, respectively. The thickness of the shell is denoted by $\Delta = a - b$. The shell is assumed to have the constitutive parameters μ_1 and ε_1 and electrical conductivity σ_1. The material inside and outside the shell is assumed to be free space with no conductivity. This material is designated as region #2, with parameters μ_2, ε_2 and $\sigma_2 = 0$. The spherical coordinate system is described by the usual (r, θ, ϕ) coordinates, as noted in the figure.

B. Representation of Fields in Spherical Coordinates

In region #1, the wave propagation constant is

$$k_1 \approx \sqrt{\frac{\omega\mu_1\sigma_1}{2}}\left(1-j\right) \quad \text{for } \sigma_1 .>> \omega\, \varepsilon_1 \tag{1a}$$

and in region #2

$$k_2 = \omega\sqrt{\mu_2\varepsilon_2}\ . \tag{1b}$$

For use later in this paper, the following ratios are defined:

$$\kappa = \frac{k_2}{k_1} \quad \text{and} \quad \Omega = \frac{\mu_2}{\mu_1}\ . \tag{1c}$$

As developed by Stratton [7] (page 414), the EM field in a spherical coordinate system can be expressed as weighted sums of spherical vector wave functions $\overline{m}^{(i)}_{\substack{e\\o}m,n}$ and $\overline{n}^{(i)}_{\substack{e\\o}m,n}$, where indices $n = 0, 1, \cdots \infty$, and $m = 0, 1, \cdots n$. The symbols *e* and *o* denote solutions that are even or odd with respect to the x axis, and the index (i) denotes the type of radial function used in the expansion. These vector wave functions are

$$\bar{m}^{(i)}_{\substack{e\\o}m,n} = \mp(-1)^m \, m z^{(i)}_n(kr) \frac{P^m_n(\cos\theta)}{\sin\theta} \begin{matrix}\sin\\ \cos\end{matrix} m\phi \, \hat{\theta} - \tag{2}$$

$$(-1)^m z^{(i)}_n(kr) \frac{\partial P^m_n(\cos\theta)}{\partial\theta} \begin{matrix}\cos\\ \sin\end{matrix} m\phi \, \hat{\phi}$$

$$\begin{aligned} \bar{n}^{(i)}_{\substack{e\\o}m,n} &= n(n+1)(-1)^m \frac{z^{(i)}_n(kr)}{kr} P^m_n(\cos\theta) \begin{matrix}\cos\\ \sin\end{matrix} m\phi \, \hat{r} \\ &+(-1)^m \frac{1}{kr}\frac{\partial}{\partial(kr)}\left[kr\, z^{(i)}_n(kr)\right] \frac{\partial P^m_n(\cos\theta)}{\partial\theta} \begin{matrix}\cos\\ \sin\end{matrix} m\phi \, \hat{\theta} \\ &\mp(-1)^m \frac{m}{kr\sin\theta}\frac{\partial}{\partial(kr)}\left[kr\, z^{(i)}_n(kr)\right] P^m_n(\cos\theta) \begin{matrix}\sin\\ \cos\end{matrix} m\phi \, \hat{\phi} \end{aligned} \tag{3}$$

where the radial function $z^{(i)}_n(kr)$ is chosen by the parameter i as

$$z^{(i)}_n(kr) = \begin{bmatrix} j_n(kr) & i=1 \\ y_n(kr) & i=2 \\ h^{(1)}_n(kr) & i=3 \\ h^{(2)}_n(kr) & i=4 \end{bmatrix}. \tag{4}$$

and k denotes the propagation constant for the specific medium in which the spherical waves are propagating.

The functions $P^m_n(x)$ in Eqs.(2) and (3) are the associated Legendre polynomials[2], which according to [19, §8.66], are defined from the Legendre polynomials $P_n(x)$ by

$$P^m_n(x) = (-1)^m (1-x^2)^{\frac{1}{2}m} \frac{d^m P_n(x)}{dx^m}. \tag{5}$$

From [8] the x-directed incident plane wave shown in Figure 1 may be written as a summation of the spherical wave functions as

$$\begin{aligned} E^i &= E_o e^{-jk_2 x}\hat{x} \\ &= E_o \sum_{n=1}^{\infty} (-j)^n \frac{2n+1}{n(n+1)} \left[\bar{m}^{(1)}_{o,1,n} + j\bar{n}^{(1)}_{e,1,n}\right] \end{aligned} \tag{6a}$$

$$H^i = -\frac{k_2}{\omega\mu_2} E_o \sum_{n=1}^{\infty} (-j)^n \frac{2n+1}{n(n+1)} \left[\bar{m}^{(1)}_{e,1,n} - j\bar{n}^{(1)}_{o,1,n}\right]. \tag{6b}$$

The scattered (or "reflected") E and H fields for $r > a$ is

$$E^r = E_o \sum_{n=1}^{\infty} (-j)^n \frac{2n+1}{n(n+1)} \left[a^r_n \bar{m}^{(4)}_{o,1,n} + jb^r_n \bar{n}^{(4)}_{e,1,n}\right] \; (r \ge a) \tag{7a}$$

$$H^r = -\frac{k_2}{\omega\mu_2} E_o \sum_{n=1}^{\infty} (-j)^n \frac{2n+1}{n(n+1)} \left[b^r_n \bar{m}^{(4)}_{e,1,n} - ja^r_n \bar{n}^{(4)}_{o,1,n}\right] \; (r \ge a) \tag{7b}$$

Note that the arguments of the radial functions in Eqs.(6) and (7) are ($k_2 a$) and the leading factor for the H-field $k_2/\omega\mu_2$ is simply the characteristic wave impedance in medium 2.

Inside the material of the spherical shell, the EM fields are represented in a similar manner, as

$$E^s = E_o \left\{ \begin{aligned} &\sum_{n=1}^{\infty} (-j)^n \frac{2n+1}{n(n+1)} \left[p_n \bar{m}^{(4)}_{o,1,n} + j q_n \bar{n}^{(4)}_{e,1,n}\right] \\ &+\sum_{n=1}^{\infty} (-j)^n \frac{2n+1}{n(n+1)} \left[d_n \bar{m}^{(3)}_{o,1,n} + j f_n \bar{n}^{(3)}_{e,1,n}\right] \end{aligned} \right\} \; (b < r < a) \tag{8a}$$

$$H^s = -\frac{k_1}{\omega\mu_1} E_o \left\{ \begin{aligned} &\sum_{n=1}^{\infty} (-j)^n \frac{2n+1}{n(n+1)} \left[q_n \bar{m}^{(4)}_{e,1,n} - jp_n \bar{n}^{(4)}_{o,1,n}\right] \\ &+\sum_{n=1}^{\infty} (-j)^n \frac{2n+1}{n(n+1)} \left[f_n \bar{m}^{(3)}_{e,1,n} - jd_n \bar{n}^{(3)}_{o,1,n}\right] \end{aligned} \right\} \; \mathit{for} \; (b < r < a) \tag{8b}$$

with the radial functions arguments being ($k_1 a$).

Inside the sphere void with $r \le b$, the field representation is

$$E^c = E_o \sum_{n=1}^{\infty} (-j)^n \frac{2n+1}{n(n+1)} \left[a^c_n \bar{m}^{(1)}_{o,1,n} + jb^c_n \bar{n}^{(1)}_{e,1,n}\right] \tag{9a}$$

$$H^c = -\frac{k_2}{\omega\mu_2} E_o \sum_{n=1}^{\infty} (-j)^n \frac{2n+1}{n(n+1)} \left[b^c_n \bar{m}^{(1)}_{e,1,n} - ja^c_n \bar{n}^{(1)}_{o,1,n}\right] \tag{9b}$$

with arguments of the radial function being ($k_2 a$).

The eight coefficients occurring in Eqs.(7-9) a^r_n, b^r_n, p_n, q_n, d_n, f_n, a^c_n and b^c_n are unknowns[3] that can be determined by the boundary conditions at the interfaces at $r = a$ and $r = b$ of the sphere. These boundary conditions are that the tangential components of E and H must be continuous through the interfaces, and are

$$\begin{aligned} \left(E^i + E^r\right)_\theta &= \left(E^s\right)_\theta \quad \text{and} \quad \left(E^i + E^r\right)_\phi = \left(E^s\right)_\phi \\ \left(H^i + H^r\right)_\theta &= \left(H^s\right)_\theta \quad \text{and} \quad \left(H^i + H^r\right)_\phi = \left(H^s\right)_\phi \end{aligned} \quad (\text{at } r = a). \tag{10}$$

The same form of boundary conditions also holds at $r = b$.

In ref. [8] where the EM fields were calculated at the center of the sphere, only the $n = 1$ case was required in the summations, At that location, higher order terms of n in the field expansions vanish. For the more general case, however, other values of n must be considered. By applying the boundary conditions independently for each value of n, one can obtain a set of eight equations relating the coefficients $a^r_n, b^r_n \cdots b^c_n$. These equations are

$$j_n(k_2 a) + a^r_n h^{(2)}_n(k_2 a) = p_n h^{(2)}_n(k_1 a) + d_n h^{(1)}_n(k_1 a) \tag{11a}$$

---

[2] It is unfortunate that there is an inconsistency in the definition of the associated Legendre polynomials in the literature. Some references, such as Abramowitz [19] include the $(-1)^m$ parameter in the definition, as shown in Eq.(5). However other authors, including Stratton, omit this factor, with the result that the definition of the vector wave functions of Eqs. (3) and (4) can vary from text to text. In this paper, we use Abramowitz's definition and have modified the wave functions of Stratton by adding the term $(-1)^m$ to Eqs. (3) and (4). Butler [20] has surveyed a number of widely used texts for their usage of this term with the following results. Those authors that use the $(-1)^m$ term include Abramowitz & Stegun, R. Harrington, D. S. Jones, Magnus & Oberhettinger and S. Schelkunoff. Authors that exclude this term include J. Van Bladel, J. Stratton, A. Sommerfeld and W. Smythe.

[3] These parameters are named in the same way as in ref. [8].

$$\left\{\left[k_2 a\, j_n(k_2 a)\right]' + b_n^r\left[k_2 a\, h_n^{(2)}(k_2 a)\right]'\right\} = \kappa\left[\, q_n\left[k_1 a\, h_n^{(2)}(k_1 a)\right]' + f_n\left[k_1 a\, h_n^{(1)}(k_1 a)\right]'\,\right] \tag{11b}$$

$$\frac{\kappa}{\Omega}\left[j_n(k_2 a) + b_n^r h_n^{(2)}(k_2 a)\right] = q_n h_n^{(2)}(k_1 a) + f_n h_n^{(1)}(k_1 a) \tag{11c}$$

$$\frac{1}{\Omega}\left\{\left[k_2 a\, j_n(k_2 a)\right]' + a_n^r\left[k_2 a\, h_n^{(2)}(k_2 a)\right]'\right\} = p_n\left[k_1 a\, h_n^{(2)}(k_1 a)\right]' + d_n\left[k_1 a\, h_n^{(1)}(k_1 a)\right]' \tag{11d}$$

$$p_n h_n^{(2)}(k_1 b) + d_n h_n^{(1)}(k_1 b) = a_n^c\, j_n(k_2 b) \tag{11e}$$

$$\kappa\left\{q_n\left[k_1 b\, h_n^{(2)}(k_1 b)\right]' + f_n\left[k_1 b\, h_n^{(1)}(k_1 b)\right]'\right\} = b_n^c\left[k_2 b\, j_n(k_2 b)\right]' \tag{11f}$$

$$\frac{\Omega}{\kappa}\left[q_n h_n^{(2)}(k_1 b) + f_n h_n^{(1)}(k_1 b)\right] = b_n j_n(k_2 b) \tag{11g}$$

$$\Omega\left\{p_n\left[k_1 b\, h_n^{(2)}(k_1 b)\right]' + d_n\left[k_1 b\, h_n^{(1)}(k_1 b)\right]'\right\} = a_n^c\left[k_2 b\, j_n(k_2 b)\right]' \tag{11h}$$

where the parameters κ and Ω have been defined in Eq.(1c). Note that the ' symbol in these expressions denotes the derivative function, as $\left[xf(x)\right]' \equiv d/dx\left(xf(x)\right)$.

C. Scaling of the Hankel Functions and Expansion Coefficients

In using the above equations for determining the expansion coefficients, a problem arises in the evaluation of the wave functions in region #1. This is due to the exponential growth of the Hankel function $h_n^{(1)}(k_1 r)$ when the argument is complex and the frequency becomes large. To see this, ref.[19, §10.1.16] provides the following representations for the spherical Hankel function of the first kind $h_n^{(1)}\left(kr\right)$

$$h_n^{(1)}(kr) = e^{jkr} j^{-n-1}(kr)^{-1}\sum_{k=0}^{n}\frac{\left(n+k\right)!}{k!\Gamma(n-k+1)}\left(-2jkr\right)^{-k} \tag{12}$$

In region #1 the propagation constant k_1 in Eq.(1a) is complex, and consequently the leading term in Eq.(12) is

$$T(k_1 r) \equiv e^{jk_1 r} = e^{j\sqrt{\frac{\omega\mu_1\sigma_1}{2}}(1-j)r} = e^{\sqrt{(\omega\mu_1\sigma_1)\mathrm{r}/2}}\, e^{j\sqrt{(\omega\mu_1\sigma_1)\mathrm{r}/2}}\,. \tag{13}$$

This exponential function becomes unbounded as ω, σ or *r* → ∞. As an example, consider the case of an aluminum shell with a radius of 1 meter. As a relatively low frequency of 1000 Hz, the exponential growth term in Eq.(13) is $e^{\sqrt{(\omega\mu_1\sigma_1)\mathrm{r}/2}} \sim e^{374}$. Thus the use of $h_n^{(1)}(ka)$ or $h_n^{(1)}(kb)$ directly in Eq.(11) becomes impossible at high frequencies due to numerical round-off errors – even if it's exponential growth may be ultimately cancelled out by a small term somewhere in a complicated expression.

In numerical calculations involving $h_n^{(1)}(k_1 r)$ it is convenient to define the *scaled* Hankel function of the first kind as

$$\hat{h}_n^{(1)}(kr) \equiv j^{-n-1}(kr)^{-1}\sum_{k=0}^{n}\frac{\left(n+k\right)!}{k!\Gamma(n-k+1)}\left(-2jkr\right)^{-k} \tag{14}$$

so that

$$h_n^{(1)}(kr) = T(kr)\,\hat{h}_n^{(1)}(kr) \tag{15}$$

Similarly, the spherical Hankel function of the second kind $h_n^{(2)}\left(kr\right)$ can be written as

$$h_n^{(2)}(kr) = e^{-jkr} j^{n+1}(kr)^{-1}\sum_{k=0}^{n}\frac{\left(n+k\right)!}{k!\Gamma(n-k+1)}\left(2jkr\right)^{-k} \equiv \frac{1}{T(kr)}\hat{h}_n^{(2)}(kr). \tag{16}$$

Equations (15) and (16) use a common scaling function T(*kr*) together with two *scaled spherical Hankel functions*[4] $\hat{h}_n^{(1)}(kr)$ and $\hat{h}_n^{(2)}(kr)$. These scaled functions maintain reasonable accuracy over a wide range of values of the complex parameter (*kr*) and they are provided as an option in many special function routines. Note that this is not an approximation to the Hankel functions, but rather, just a factorization of the functions.

To avoid numerical overflow problems in solving the set of equations of Eqs.(11a–h), we express the boundary conditions and Hankel functions in region #1 using the scaled spherical Hankel functions and the appropriate scaling factors as

$$h_n^{(1)}(k_1 a) = T(k_1 a)\,\hat{h}_n^{(1)}(k_1 a);\;\; h_n^{(2)}(k_1 a) = \frac{1}{T\left(k_1 a\right)}\hat{h}_n^{(2)}(k_1 a) \tag{17a}$$

$$h_n^{(1)}(k_1 b) = T(k_1\ \mathrm{b})\hat{h}_n^{(1)}(k_1 b);\;\; h_n^{(2)}(k_1 b) = \frac{1}{T(k_1\ \mathrm{b})}\hat{h}_n^{(2)}(k_1 b). \tag{17b}$$

With these scaled Hankel functions for region #1, the boundary conditions in Eqs.(11) can be written in a compact matrix form as shown in Eq.(18) on the next page.

---

[4] In this paper, any parameter or function with the ^ symbol is designated as a scaled quantity.

$$\begin{bmatrix}
-h_n^{(2)}(k_2a) & 0 & \frac{1}{T(k_1a)}h_n^{(2)}(k_1a) & 0 & T(k_1a)\hat{h}_n^{(1)}(k_1a) & 0 & 0 & 0 \\
0 & -\left[k_2a\,h_n^{(2)}(k_2a)\right]' & 0 & \frac{\kappa}{T(k_1a)}\left[k_1a\,\hat{h}_n^{(2)}(k_1a)\right]' & 0 & T(k_1a)\kappa\left[k_1a\,\hat{h}_n^{(1)}(k_1a)\right]' & 0 & 0 \\
0 & -\frac{\kappa}{\Omega}\hat{h}_n^{(2)}(k_2a) & 0 & \frac{1}{T(k_1a)}\hat{h}_n^{(2)}(k_1a) & 0 & T(k_1a)\hat{h}_n^{(1)}(k_1a) & 0 & 0 \\
-\frac{1}{\Omega}\left[k_2a\,h_n^{(2)}(k_2a)\right]' & 0 & \frac{1}{T(k_1a)_1}\left[k_1a\,\hat{h}_n^{(2)}(k_1a)\right]' & 0 & T(k_1a)\left[k_1a\,\hat{h}_n^{(1)}(k_1a)\right]' & 0 & 0 & 0 \\
0 & 0 & \frac{1}{T(k_1b)}\hat{h}_n^{(2)}(k_1b) & 0 & T(k_1b)\hat{h}_n^{(1)}(k_1b) & 0 & -j_n\left(k_2b\right) & 0 \\
0 & 0 & 0 & \frac{1}{T(k_1b)}\kappa\left[k_1b\,\hat{h}_n^{(2)}(k_1b)\right]' & 0 & T(k_1b)\kappa\left[k_1b\,\hat{h}_n^{(1)}(k_1b)\right]' & 0 & -\left[k_2b\;j_n\left(k_2b\right)\right]' \\
0 & 0 & 0 & \frac{1}{T(k_1b)}\frac{\Omega}{\kappa}\hat{h}_n^{(2)}(k_1b) & 0 & T(k_1b)\frac{\Omega}{\kappa}\hat{h}_n^{(1)}(k_1b) & 0 & -j_n\left(k_2b\right) \\
0 & 0 & \frac{1}{T(k_1b)}\Omega\left[k_1b\,\hat{h}_n^{(2)}(k_1\,\mathrm{b})\right]' & 0 & T(k_1b)\Omega\left[k_1b\;\hat{h}_n^{(1)}(k_1b)\right]' & 0 & -\left[k_2b\;j_n\left(k_2b\right)\right]' & 0
\end{bmatrix}
\begin{bmatrix} a_n^r \\ b_n^r \\ p_n \\ q_n \\ d_n \\ f_n \\ a_n^c \\ b_n^c \end{bmatrix}
=
\begin{bmatrix} j_n\left(k_2a\right) \\ \left[k_2a j_n\left(k_2a\right)\right]' \\ \frac{\kappa}{\Omega}j_n\left(k_2a\right) \\ \frac{1}{\Omega}\left[k_2a j_n\left(k_2a\right)\right]' \\ 0 \\ 0 \\ 0 \\ 0 \end{bmatrix}
\tag{18}$$

$$\begin{aligned}
Den1_n =& \frac{T(k_1b)}{T(k_1a)}\left[\left(\Omega\, j_n(k_2b)\left[k_1b\,\hat{h}_n^{(1)}(k_1b)\right]' - \left[k_2b\, j_n(k_2b)\right]'\,\hat{h}_n^{(1)}(k_1b)\right)\left(\hat{h}_n^{(2)}(k_1a)\left[k_2a\,h_n^{(2)}(k_2a)\right]' - \Omega\; h_n^{(2)}(k_2a)\left[k_1a\,\hat{h}_n^{(2)}(k_1a)\right]'\right)\right] \\
&+\frac{T(k_1a)}{T(\mathrm{k}_1\mathrm{b})}\left[\left(\Omega\, j_n(k_2b)\left[k_1b\,\hat{h}_n^{(2)}(k_1b)\right]' - \left[k_2b\, j_n(k_2b)\right]'\,\hat{h}_n^{(2)}(k_1b)\right)\left(\Omega\; h_n^{(2)}(k_2a)\left[k_1a\,\hat{h}_n^{(1)}(k_1a)\right]' - \hat{h}_n^{(1)}(k_1a)\left[k_2a\,h_n^{(2)}(k_2a)\right]'\right)\right] \\
&\equiv \frac{1}{T\left(k_1\Delta\right)}A_1 + T\left(k_1\Delta\right)B_1 \approx T\left(k_1\Delta\right)B_1 \quad \text{for} \left|\frac{T(k_1a)}{T(k_1b)}\right| = \left|e^{jk_1(a-b)}\right| \equiv \left|T\left(k_1\Delta\right)\right| >> 1/\left|T\left(k_1\Delta\right)\right|
\end{aligned}\tag{19a}$$

$$\begin{aligned}
Den2_n =& \frac{T(k_1b)}{T(k_1a)}\left[\left(\kappa^2 j_n(k_2b)\left[k_1b\,\hat{h}_n^{(1)}(k_1b)\right]' - \Omega\left[k_2b\, j_n(k_2b)\right]'\,\hat{h}_n^{(1)}(k_1b)\right)\left(\Omega\,\hat{h}_n^{(2)}(k_1a)\left[k_2a\,h_n^{(1)}(k_2a)\right]' - \kappa^2\, h_n^{(2)}(k_2a)\left[k_1a\,\hat{h}_n^{(2)}(k_1a)\right]'\right)\right] \\
&+\frac{T(k_1a)}{T(k_1b)}\left[\left(\kappa^2 j_n(k_2b)\left[k_1b\,\hat{h}_n^{(2)}(k_1b)\right]' - \Omega\left[k_2b\, j_n(k_2b)\right]'\,\hat{h}_n^{(2)}(k_1b)\right)\left(\kappa^2\, h_n^{(2)}(k_2a)\left[k_1a\,\hat{h}_n^{(2)}(k_1a)\right]' - \Omega\,\hat{h}_n^{(1)}(k_1a)\left[k_2a\,h_n^{(2)}(k_2a)\right]'\right)\right] \\
&\equiv \frac{1}{T\left(k_1\Delta\right)}A_2 + T\left(k_1\Delta\right)B_2 \approx T\left(k_1\Delta\right)B_2 \quad \text{for} \left|\frac{T(k_1a)}{T(k_1b)}\right| = \left|e^{jk_1(a-b)}\right| \equiv \left|T\left(k_1\Delta\right)\right| >> 1/\left|T\left(k_1\Delta\right)\right|
\end{aligned}\tag{19b}$$

To observe the effects of using the scaled Hankel functions and to provide an alternative to a strict numerical inversion of Eq.(18) for each value of the summation parameter *n*, one can develop closed-form expressions for the expansion coefficients. Reference [8] provides expressions for the coefficients a_1^c and b_1^c for the E-fields at the center of the sphere and here we generalize their results for arbitrary *n* and for all regions. It should also be mentioned that Baum [11] in his Appendix A also provides expressions for the expansion coefficients, but not in stand-alone terms. He provides ratios of coefficients, relative to the coefficients of the incident plane wave.

Obtaining a symbolic solution is tedious but it can be assisted by using a symbolic solver to invert Eq.(18) and obtain algebraic expressions for the coefficients. In doing this there are two terms that occur in the denominators of the various expressions for the coefficients. These are denoted as $Den1_n$ and $Den2_n$ and are given in Eqs.(19a and 19b.)

Note that the functions $Den1_n$ and $Den2_n$ depend on the ratio of scaling functions $T(k_1a)/T(k_1b) = e^{jk_2(a-b)} = T(k_1\Delta)$. The bracketed terms A_1, A_2, B_1 and B_2 contain scaled Hankel functions $\hat{h}_n^{(1)}(k_1a)$, $\hat{h}_n^{(2)}(k_1a)$, $\hat{h}_n^{(1)}(k_1b)$ and $\hat{h}_n^{(2)}(k_1b)$, as well as unscaled functions $j_n(k_2b)$ and $h_n^{(2)}(k_2a)$. These bracketed terms can be calculated easily at high frequencies, with no problems with numerical overflow. The leading coefficient $T(k_1\Delta)$ still diverges at high frequencies, but not as rapidly as $T(k_1a)$ or $T(k_1b)$. This divergence must be offset by a similar decreasing exponential term in the expression for the EM fields, as will be discussed in Section II.D.3.

At low frequencies, or for very thin shell walls $|k_1\Delta|$ is small and the denominator terms $Den1_n$ and $Den2_n$ can be evaluated directly as written in Eqs.(19). However as $|k_1\Delta|$ becomes large so that $\left|T(k_1\Delta)\right| >> 1/\left|T(k_1\Delta)\right|$ approximate expression for these denominator terms can be used.

The eight expansion coefficients a_n^r, b_n^r, p_n, q_n, d_n, f_n, a_n^c and b_n^c are given in closed form in Eqs.(20) – (27), which are provided in Table 1. For each coefficient the complete form and the high frequency approximation are given. Some of these expressions have been simplified somewhat through the use of appropriate Wronskian relationships between the radial functions. Reference [11] also discusses this simplification. If Ω = 1 (for a non-magnetic shell material), additional simplifications are possible using the Wronskian relationships.

Table 1. Closed form expressions for the eight expansion coefficients.

Coeff.	**Value**	**Approximation for $\lvert T(k_1\Delta)\rvert >> 1/\lvert T(k_1\Delta)\rvert$**	**Eq.**
a_n^r	$-\frac{1}{Den1_n}\frac{1}{T(k_1\Delta)}\begin{bmatrix}\left(\hat{h}_n^{(2)}(k_1a)\left[k_2a\,j_n(k_2a)\right]' - \Omega\, j_n(k_2a)\left[k_1a\,\hat{h}_n^{(2)}(k_1a)\right]'\right) \\ \left(\Omega\, j_n(k_2b)\left[k_1b\,\hat{h}_n^{(1)}(k_1b)\right]' - \hat{h}_n^{(1)}(k_1b)\left[k_2b\,j_n(k_2b)\right]'\right)\end{bmatrix}$ $-\frac{1}{Den1_n}T(k_1\Delta)\begin{bmatrix}\left(\hat{h}_n^{(1)}(k_1a)\left[k_2a\,j_n(k_2a)\right]' - \Omega\, j_n(k_2a)\left[k_1a\,\hat{h}_n^{(1)}(k_1a)\right]'\right)\times \\ \left(\hat{h}_n^{(2)}(k_1b)\left[k_2b\,j_n(k_2b)\right]' - \Omega\, j_n(k_2b)\left[k_1b\,\hat{h}_n^{(2)}(k_1b)\right]'\right)\end{bmatrix}$	$-\frac{\begin{bmatrix}\left(\hat{h}_n^{(1)}(k_1a)\left[k_2a\,j_n(k_2a)\right]' - \Omega\, j_n(k_2a)\left[k_1a\,\hat{h}_n^{(1)}(k_1a)\right]'\right)\times \\ \left(\hat{h}_n^{(2)}(k_1b)\left[k_2b\,j_n(k_2b)\right]' - \Omega\, j_n(k_2b)\left[k_1b\,\hat{h}_n^{(2)}(k_1b)\right]'\right)\end{bmatrix}}{\begin{bmatrix}\left(\Omega\, j_n(k_2b)\left[k_1b\,\hat{h}_n^{(2)}(k_1b)\right]' - \left[k_2b\,j_n(k_2b)\right]'\,\hat{h}_n^{(2)}(k_1b)\right)\times \\ \left(\Omega\, h_n^{(2)}(k_2a)\left[k_1a\,\hat{h}_n^{(1)}(k_1a)\right]' - \hat{h}_n^{(1)}(k_1a)\left[k_2a\,h_n^{(2)}(k_2a)\right]'\right)\end{bmatrix}}$	(20)
b_n^r	$-\frac{1}{Den2_n}\frac{1}{T(k_1\Delta)}\begin{bmatrix}\left(\Omega\,\hat{h}_n^{(2)}(k_1a)\left[k_2a\,j_n(k_2a)\right]' - \kappa^2 j_n(k_2a)\left[k_1a\,\hat{h}_n^{(2)}(k_1a)\right]'\right)\times \\ \left(\kappa^2 j_n(k_2b)\left[k_1b\,\hat{h}_n^{(1)}(k_1b)\right]' - \Omega\,\hat{h}_n^{(1)}(k_1b)\left[k_2b\,j_n(k_2b)\right]'\right)\end{bmatrix}$ $-\frac{1}{Den2_n}T(k_1\Delta)\begin{bmatrix}\left(\kappa^2 j_n(k_2a)\left[k_1a\,\hat{h}_n^{(1)}(k_1a)\right]' - \Omega\,\hat{h}_n^{(1)}(k_1a)\left[k_2a\,j_n(k_2a)\right]'\right)\times \\ \left(\kappa^2 j_n(k_2b)\left[k_1b\,\hat{h}_n^{(2)}(k_1b)\right]' - \Omega\,\hat{h}_n^{(2)}(k_1b)\left[k_2b\,j_n(k_2b)\right]'\right)\end{bmatrix}$	$-\frac{\begin{bmatrix}\left(\kappa^2 j_n(k_2a)\left[k_1a\,\hat{h}_n^{(1)}(k_1a)\right]' - \Omega\,\hat{h}_n^{(1)}(k_1a)\left[k_2a\,j_n(k_2a)\right]'\right)\times \\ \left(\kappa^2 j_n(k_2b)\left[k_1b\,\hat{h}_n^{(2)}(k_1b)\right]' - \Omega\,\hat{h}_n^{(2)}(k_1b)\left[k_2b\,j_n(k_2b)\right]'\right)\end{bmatrix}}{\begin{bmatrix}\left(\kappa^2 j_n(k_2b)\left[k_1b\,\hat{h}_n^{(2)}(k_1b)\right]' - \Omega\left[k_2b\,j_n(k_2b)\right]'\,\hat{h}_n^{(2)}(k_1b)\right)\times \\ \left(\kappa^2 h_n^{(2)}(k_2a)\left[k_1a\,\hat{h}_n^{(2)}(k_1a)\right]' - \Omega\,\hat{h}_n^{(1)}(k_1a)\left[k_2a\,h_n^{(2)}(k_2a)\right]'\right)\end{bmatrix}}$	(21)
p_n	$-\frac{1}{Den1_n}T(k_1b)\left[\left(\frac{-j}{k_2a}\right)\begin{pmatrix}\hat{h}_n^{(1)}(k_1b)\left[k_2b\,j_n(k_2b)\right]' - \\ \Omega\, j_n(k_2b)\left[k_1b\,\hat{h}_n^{(1)}(k_1b)\right]'\end{pmatrix}\right]$	$-\frac{T(k_1b)}{T(k_1\Delta)}\frac{\left[\left(\frac{-j}{k_2a}\right)\begin{pmatrix}\hat{h}_n^{(1)}(k_1b)\left[k_2b\,j_n(k_2b)\right]' - \\ \Omega\, j_n(k_2b)\left[k_1b\,\hat{h}_n^{(1)}(k_1b)\right]'\end{pmatrix}\right]}{\begin{bmatrix}\left(\Omega\, j_n(k_2b)\left[k_1b\,\hat{h}_n^{(2)}(k_1b)\right]' - \left[k_2b\,j_n(k_2b)\right]'\,\hat{h}_n^{(2)}(k_1b)\right)\times \\ \left(\Omega\, h_n^{(2)}(k_2a)\left[k_1a\,\hat{h}_n^{(1)}(k_1a)\right]' - \hat{h}_n^{(1)}(k_1a)\left[k_2a\,h_n^{(2)}(k_2a)\right]'\right)\end{bmatrix}}$ *or* $-\frac{T(k_1b)}{T(k_1\Delta)}\hat{p}_n$	(22)

Coeff.	Value	Approximation for |*T*(*k₁Δ*)| >> 1/|*T*(*k₁Δ*)|	Eq.
q_n	$-\frac{\kappa}{Den2_n}T(k_1b)\left[\left(\frac{-j}{k_2a}\right)\left(\begin{array}{l}\Omega\,\hat{h}_n^{(1)}(k_1b)\left[k_2b\,j_n(k_2b)\right]' - \\ \kappa^2 j_n(k_2b)\left[k_1b\,\hat{h}_n^{(1)}(k_1b)\right]'\end{array}\right)\right]$	$-\frac{T(k_1b)}{T(k_1\Delta)}\frac{\left[\kappa\left(\frac{-j}{k_2a}\right)\left(\begin{array}{l}\Omega\,\hat{h}_n^{(1)}(k_1b)\left[k_2b\,j_n(k_2b)\right]' - \\ \kappa^2 j_n(k_2b)\left[k_1b\,\hat{h}_n^{(1)}(k_1b)\right]'\end{array}\right)\right]}{\left[\begin{array}{l}\left(\kappa^2 j_n(k_2b)\left[k_1b\,\hat{h}_n^{(2)}(k_1b)\right]' - \Omega\left[k_2b\,j_n(k_2b)\right]'\,\hat{h}_n^{(2)}(k_1b)\right)\times \\ \left(\kappa^2 h_n^{(2)}(k_2a)\left[k_1a\,\hat{h}_n^{(2)}(k_1a)\right]' - \Omega\,\hat{h}_n^{(1)}(k_1a)\left[k_2a\,h_n^{(2)}(k_2a)\right]'\right)\end{array}\right]}$ *or* $-\frac{T(k_1b)}{T(k_1\Delta)}\hat{q}_n$	(23)
d_n	$\frac{1}{Den1_n}\frac{1}{T(k_1b)}\left[\left(\frac{-j}{k_2a}\right)\left(\begin{array}{l}\hat{h}_n^{(2)}(k_1b)\left[k_2b\,j_n(k_2b)\right]' - \\ \Omega\,j_n(k_2b)\left[k_1b\,\hat{h}_n^{(2)}(k_1b)\right]'\end{array}\right)\right]$	$\frac{1}{T(k_1\Delta)T(k_1b)}\frac{\left[\left(\frac{-j}{k_2a}\right)\left(\begin{array}{l}\hat{h}_n^{(2)}(k_1b)\left[k_2b\,j_n(k_2b)\right]' - \\ \Omega\,j_n(k_2b)\left[k_1b\,\hat{h}_n^{(2)}(k_1b)\right]'\end{array}\right)\right]}{\left[\begin{array}{l}\left(\Omega\,j_n(k_2b)\left[k_1b\,\hat{h}_n^{(2)}(k_1b)\right]' - \left[k_2b\,j_n(k_2b)\right]'\,\hat{h}_n^{(2)}(k_1b)\right)\times \\ \left(\Omega\,h_n^{(2)}(k_2a)\left[k_1a\,\hat{h}_n^{(1)}(k_1a)\right]' - \hat{h}_n^{(1)}(k_1a)\left[k_2a\,h_n^{(2)}(k_2a)\right]'\right)\end{array}\right]}$ *or* $\frac{1}{T(k_1\Delta)T(k_1b)}\hat{d}_n$	(24)
f_n	$\frac{\kappa}{Den2_n}\frac{1}{T(k_1b)}\left[\left(\frac{-j}{k_2a}\right)\left(\begin{array}{l}\Omega\,\hat{h}_n^{(2)}(k_1b)\left[k_2b\,j_n(k_2b)\right]' - \\ \kappa^2 j_n(k_2b)\left[k_1b\,\hat{h}_n^{(2)}(k_1b)\right]'\end{array}\right)\right]$	$\frac{1}{T(k_1\Delta)T(k_1b)}\frac{\left[\kappa\left(\frac{-j}{k_2a}\right)\left(\begin{array}{l}\Omega\,\hat{h}_n^{(2)}(k_1b)\left[k_2b\,j_n(k_2b)\right]' - \\ \kappa^2 j_n(k_2b)\left[k_1b\,\hat{h}_n^{(2)}(k_1b)\right]'\end{array}\right)\right]}{\left[\begin{array}{l}\left(\kappa^2 j_n(k_2b)\left[k_1b\,\hat{h}_n^{(2)}(k_1b)\right]' - \Omega\left[k_2b\,j_n(k_2b)\right]'\,\hat{h}_n^{(2)}(k_1b)\right)\times \\ \left(\kappa^2 h_n^{(2)}(k_2a)\left[k_1a\,\hat{h}_n^{(2)}(k_1a)\right]' - \Omega\,\hat{h}_n^{(1)}(k_1a)\left[k_2a\,h_n^{(2)}(k_2a)\right]'\right)\end{array}\right]}$ *or* $\frac{1}{T(k_1\Delta)T(k_1b)}\hat{f}_n$	(25)
a_n^c	$\frac{\Omega}{Den1_n}\left(\frac{-j}{k_2a}\right)\left(\frac{2j}{k_1b}\right)$	$\frac{1}{T(k_1\Delta)}\frac{\Omega\left(\frac{-j}{k_2a}\right)\left(\frac{2j}{k_1b}\right)}{\left[\begin{array}{l}\left(\Omega\,j_n(k_2b)\left[k_1b\,\hat{h}_n^{(2)}(k_1b)\right]' - \left[k_2b\,j_n(k_2b)\right]'\,\hat{h}_n^{(2)}(k_1b)\right)\times \\ \left(\Omega\,h_n^{(2)}(k_2a)\left[k_1a\,\hat{h}_n^{(1)}(k_1a)\right]' - \hat{h}_n^{(1)}(k_1a)\left[k_2a\,h_n^{(2)}(k_2a)\right]'\right)\end{array}\right]}$	(26)
b_n^c	$\frac{\Omega\kappa^2}{Den2_n}\left(\frac{-j}{k_2a}\right)\left(\frac{2j}{k_1b}\right)$	$\frac{1}{T(k_1\Delta)}\frac{\Omega\kappa^2\left(\frac{-j}{k_2a}\right)\left(\frac{2j}{k_1b}\right)}{\left[\begin{array}{l}\left(\kappa^2 j_n(k_2b)\left[k_1b\,\hat{h}_n^{(2)}(k_1b)\right]' - \Omega\left[k_2b\,j_n(k_2b)\right]'\,\hat{h}_n^{(2)}(k_1b)\right)\times \\ \left(\kappa^2 h_n^{(2)}(k_2a)\left[k_1a\,\hat{h}_n^{(2)}(k_1a)\right]' - \Omega\,\hat{h}_n^{(1)}(k_1a)\left[k_2a\,h_n^{(2)}(k_2a)\right]'\right)\end{array}\right]}$	(27)

Notes: $T\left(k_1\Delta\right) = e^{jk_2(a-b)}$

$T\left(k_1b\right) = e^{jk_2b}$

Den1ₙ and Den2ₙ are defined in Eqs(19a-b)

D. Evaluation of the EM fields in and around the sphere.

The eight expansion coefficients shown in Table 1 can be used with the wave expansions in Eqs.(6) – (9) to determine the EM fields in and around the sphere. These calculations will be described briefly below.

1) Outside the sphere (r > a).

In this region the EM field is the sum of the incident and sphere-scattered fields given in Eqs.(6) and (7), respectively. For the incident fields only the Bessel function $j_n(k_2 r)$ is used in the vector wave functions $\bar{m}^{(1)}_{o,1,n}$ and $\bar{n}^{(1)}_{e,1,n}$ in Eq.(6). For the scattered fields, the outward propagating Hankel function $h^{(2)}_n(k_2 r)$ appears in the vector functions $\bar{m}^{(4)}_{o,1,n}$ and $\bar{n}^{(4)}_{e,1,n}$.

The sums for the incident EM field in Eq.(6a-b) can be evaluated with no difficulty. Similarly, Eqs.(7a-b) for the scattered fields can be summed directly as the expansion coefficients a^r_n and b^r_n are easily evaluated with no overflow problems.

2) Inside the spherical cavity (r < b)

In this region the expansion coefficients a^c_n and b^c_n are used in Eqs.(9a-b) to evaluate the fields. The vector wave functions $\bar{m}^{(1)}_{\substack{e\\o}m,n}$ and $\bar{n}^{(1)}_{\substack{e\\o}m,n}$ for this calculation all contain the Bessel function $j_n(k_2 r)$, which is well behaved at high frequencies and is easy to evaluate. The expansion coefficients are given in Eqs.(26) and (27) in Table 1, and the high frequency approximations for both are seen to have a term $1/T\left(k_1\Delta\right) = e^{-jk_2\Delta}$, which is exponentially decreasing at high frequencies. This is as expected, since the internal field in the sphere should be highly attenuated at high frequencies or with thick shield walls.

3) Inside the spherical shell material (b < r< a)

For a field observation point inside the spherical shell material, the p_n and q_n parameters in Eq.(8) are always multiplied by the $h^{(2)}_n(k_1 r)$ terms contained in the $\bar{m}^{(4)}_{\substack{e\\o}m,n}$ and $\bar{n}^{(4)}_{\substack{e\\o}m,n}$ vector wave functions. Likewise, parameters d_n and f_n occur together with $h^{(1)}_n(k_1 r)$ functions contained in $\bar{m}^{(3)}_{\substack{e\\o}m,n}$ and $\bar{n}^{(3)}_{\substack{e\\o}m,n}$. In these vector functions, we can extract the exponential terms of the Hankel functions and use the scaled Hankel functions to compute the *scaled* vector wave functions denoted as $\hat{\bar{m}}^{(3)}_{\substack{e\\o}m,n}, \hat{\bar{m}}^{(4)}_{\substack{e\\o}m,n}$, $\hat{\bar{n}}^{(3)}_{\substack{e\\o}m,n}$ and $\hat{\bar{n}}^{(4)}_{\substack{e\\o}m,n}$ from Eqs.(2) and (3). For these scaled vector functions the Hankel function scaling terms T(k_1r) and 1/T(k_1r) are used to express the vector functions as

$$\bar{m}^{(3)}_{\substack{e\\o}m,n} = T(k_1 r)\, \hat{\bar{m}}^{(3)}_{\substack{e\\o}m,n} \tag{28a}$$

$$\bar{n}^{(3)}_{\substack{e\\o}m,n} = T(k_1 r)\, \hat{\bar{n}}^{(3)}_{\substack{e\\o}m,n} \tag{28b}$$

$$\bar{m}^{(4)}_{\substack{e\\o}m,n} = \frac{1}{T(k_1 r)} \hat{\bar{m}}^{(4)}_{\substack{e\\o}m,n} \tag{28c}$$

$$\bar{n}^{(4)}_{\substack{e\\o}m,n} = \frac{1}{T(k_1 r)} \hat{\bar{n}}^{(4)}_{\substack{e\\o}m,n} \tag{28d}$$

Equations (22)-(25) define normalized expansion coefficients $\hat{p}_n$, $\hat{q}_n$, $\hat{d}_n$, $\hat{f}_n$, together with the normalizing factors $T(k_1 b)/T\left(k_1\Delta\right)$ and $1/\left(T(k_1 b)T\left(k_1\Delta\right)\right)$. Using these expressions, along with normalized vectors wave functions in Eqs.(28), and introducing an alternate measure of the EM field observation point ξ inside the shell, relative to the inner radius, *b*, as *r* = *b* + *ξ*, we can express the EM fields within the shell material as

$$E^s = E_o \left\{ \begin{aligned} &\sum_{n=1}^{\infty} (-j)^n \frac{2n+1}{n(n+1)} e^{-jk_1(\Delta+\xi)} \left[\hat{p}_n\, \hat{\bar{m}}^{(4)}_{o,1,n} + j\, \hat{q}_n\, \hat{\bar{n}}^{(4)}_{e,1,n} \right] \\ +&\sum_{n=1}^{\infty} (-j)^n \frac{2n+1}{n(n+1)} e^{-jk_1(\Delta-\xi)} \left[\hat{d}_n\, \hat{\bar{m}}^{(3)}_{o,1,n} + j\, \hat{f}_n\, \hat{\bar{n}}^{(3)}_{e,1,n} \right] \end{aligned} \right\} \tag{29a}$$

$$H^s = -\frac{k_1}{\omega\mu_1} E_o \left\{ \begin{aligned} &\sum_{n=1}^{\infty} (-j)^n \frac{2n+1}{n(n+1)} e^{-jk_1(\Delta+\xi)} \left[\hat{q}_n\, \hat{\bar{m}}^{(4)}_{e,1,n} - j\hat{p}_n\, \hat{\bar{n}}^{(4)}_{o,1,n} \right] \\ +&\sum_{n=1}^{\infty} (-j)^n \frac{2n+1}{n(n+1)} e^{-jk_1(\Delta-\xi)} \left[\hat{f}_n\, \hat{\bar{m}}^{(3)}_{e,1,n} - j\hat{d}_n\, \hat{\bar{n}}^{(3)}_{o,1,n} \right] \end{aligned} \right\} \tag{29b}$$

for $(0 \le \xi \le a)$

The summations in Eqs.(29) are well behaved and easy to evaluate. This scaling procedure permits the computation of the E-fields over a broad frequency range, which is impossible with the conventional wave expansion of Eq.(8).

E. Numerical Results

A computer program was developed to evaluate Eqs.(6), (7), (9) and (29) using the closed form expressions for the expansion coefficients. To check of these calculations it was verified that the various boundary conditions on the sphere were met and that the overall behavior of the E-fields was correct.

As an additional check, the E-field and H-field transfer functions at the center of an aluminum shell (σ = 3.54 x 10^7 S/m) with radius *a* = 0.914 m (36 in) and thicknesses Δ = 0.794, 1.587 and 3.175 mm (corresponding to 1/32, 1/16 and 1/8 inches) were computed. These dimensions correspond to the same ones used in [8]. For this comparison, transfer functions relating the total E and H-field magnitudes to the magnitude of the incident E-field are defined as

$$TE(\text{dB}) = 20\log\left[\frac{\left|\vec{E}(r,\theta,\phi)\right|}{E_o}\right] \text{ and } TH(\text{dB}) = 20\log\left[\frac{\left|\vec{H}(r,\theta,\phi)\right| / E_o}{1(\text{Siemen})}\right] \tag{30}$$

In Eq.(30), the argument of the log function for TE is unitless. For TH the ratio H/E has the dimension of Siemens, so TH is defined relative to 1 Siemen. This latter transfer function definition is not ideal, but it has been used to permit a direct comparison with the results given in [8]. Figure 2 presents plots of the E-field and H-field transfer functions, expressed in dB, at the center of the aluminum sphere with different shell thicknesses, Δ. These plots are identical with those in ref. [8], and this serves as a partial validation of the present computational procedure. Note that usually the H-field transfer function is shown relative to the incident H-field, not the E-field, and at low frequencies, $H/H_0 \rightarrow 0$ dB. The low frequency limit in Figure 2a is –51.53 dB, which is exactly $1/Z_0$ expressed in dB relative to 1 Siemen.

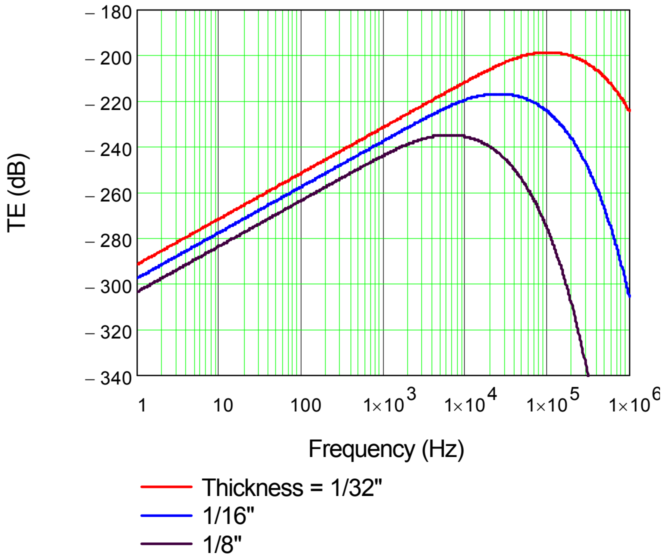

a. Electric field

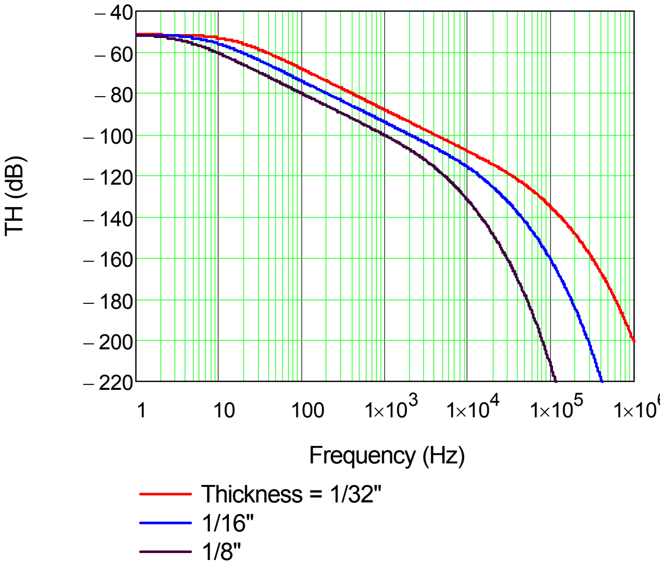

b. Magnetic field

Figure 2. Plots of the total E-field and H-field transfer functions at the center of an aluminum sphere with $a = 0.914$ m for different shell thicknesses, Δ. (Compare with Figures 2 and 8 of ref. [8].)

It is interesting to note that the upper frequency response of the transfer functions in Figure 2 is 1 MHz. Even for this relatively low frequency, the spherical wave function series is difficult to evaluate without scaling the Hankel functions. To illustrate the robustness of the present scaled solution at higher frequencies, Figure 3a presents a plot of the E-field transfer functions for the sphere for frequencies up to 1 GHz. The responses are reasonable in appearance, and if one carefully examines the transfer function for the thinnest shell, a hint of small peaks in the curves are seen at frequencies above about 200 MHz.

Figure 3b plots the transfer function for the thinnest shell on a linear scale and these peaks are seen more clearly. These peaks are due to the internal resonances in the shell. Since the shell material is highly conducting, we expect that these resonances will occur close to the classical internal resonances of a perfectly conducting sphere. According to Harrington [21, §6-2], such internal resonances occur at the roots of $J_n(k_2 b) = 0$ for the TE modes, and at the roots of $[k_2 b\, J_n(k_2 b)]' = 0$ for the TM modes.

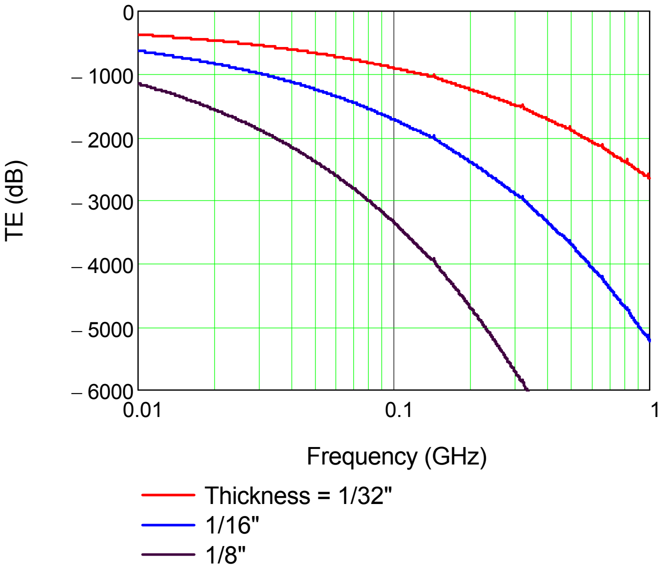

a. TE for three different shell thicknesses.

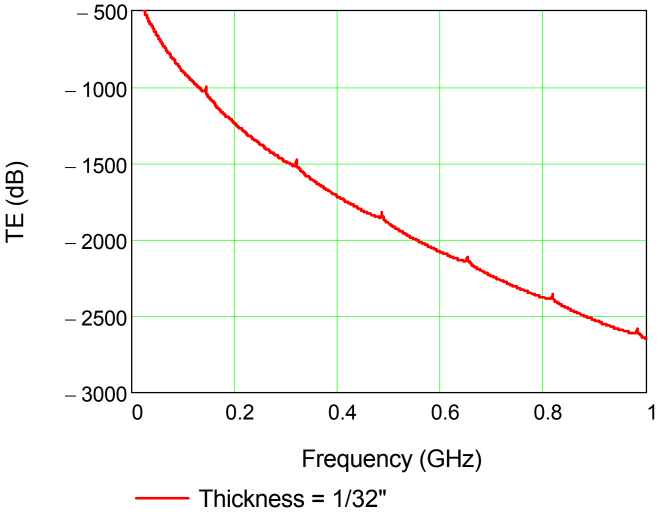

b. Linear plot of TE for a shell of thickness $\Delta = 1/32$ in.

Figure 3. Plots of the total E-field transfer function at the center of the spherical shell for higher frequencies up to 1 GHz.

Table 2 presents the computed roots for the first four TM modes, along with the resulting resonant frequencies for the sphere with a radius of about 0.914 m. We note that the agreement with the frequencies of the resonances in Figure 3b is very good. Of course, since the conductivity of the shell is so high, the internal E-field is extremely small – 1000 to 2000 dB down from the incident field.

Table 2. Interior TM resonances for a perfectly conducting shell.

No.	k_2b	Freq. (GHz)
1	2.744	0.143
2	6.117	0.320
3	9.317	0.487
4	12.486	0.653

The primary motive for this study is to understand the behavior of the internal E- and H-fields within the shell. Using the same spherical shell as in the previous example, the transfer functions for the individual components of the E- and H-fields have been evaluated along the radial path in the direction defined by the angles $\theta = 90^{\text{o}}$ and $\phi = 45^{\text{o}}$. With reference to Figure 1, this path is in the *x*-*y* plane at $z = 0$ and at an angle of 45^{o} to the *x* axis. Figure 4 shows these E-fields as a function of normalized radial distance *r/b* from the origin to *r/b* = 2 for a frequency of *f* = 100 kHz.

The important thing to observe from this plot is that for both the E- and H-fields inside the shell, there are observable spatial variations in the E-field components. For the H-field, the H_r and H_θ components are equal in magnitude (on this particular radial trajectory), but there is a definite variation of the H_ϕ component. For the E-field, the principal component is E_θ and its spatial variation is significant. Outside the sphere both the E- and H-fields approach the incident field at distances of $r/b \approx 2$.

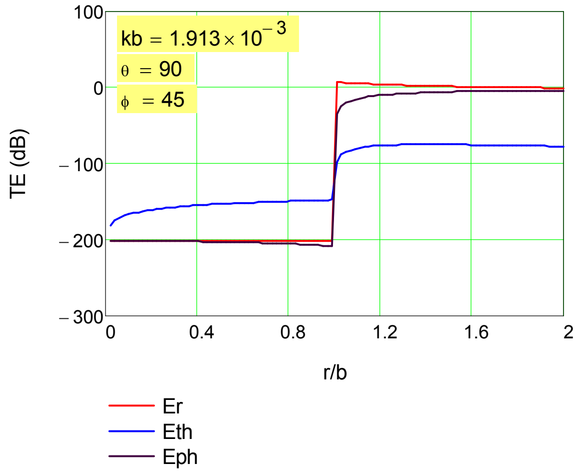

a. Electric field

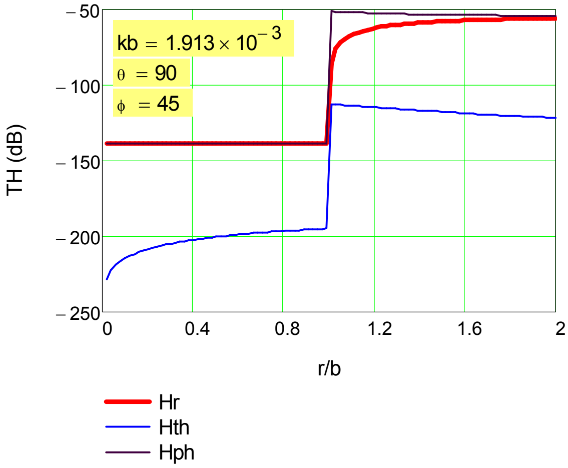

b. Magnetic field

Figure 4. E- and H-field transfer functions for the *r*, θ and ϕ field components for the spherical shell of inner radius $b = 0.914$ m and shell thickness $\Delta = 0.794$ mm, at a frequency of 100 kHz. (These E-fields are shown as a function of radial distance on a path defined by the angles $\theta = 90^{\text{o}}$ and $\phi = 45^{\text{o}}$.)

Perhaps a more intuitive measure of the internal shell fields is the total E and H-field transfer functions given by Eq.(30). Figure 5 illustrates the behavior of the E-field transfer functions in the equatorial ($z = 0$) plane along different trajectories defined by the angle ϕ. Parameters are the same as in the previous example: $b = 0.914$ m, $\Delta = 0.794$ mm, and $f = 100$ kHz.

In this figure, it is clear that the total internal H-field in the shell is constant for all practical purposes. However, there can be a significant variation of the total E-field inside the shell – about 60 dB, or a factor of 1000. Furthermore, we see that the value of TE for this shield reported in ref. [8] (at the center of the shell) is about – 198 dB. This is clearly not a representative measure of the overall shielding provided by the shell.

Another way of visualizing the EM field distribution in and around the shell it to plot the total field transfer functions in contour plots. This is done in Figure 6 for TE and in Figure 7 for TH. In these figures we note that for all practical purposes the H-field is uniform within the shell. However, this is not the case for the E-field transfer function, where the TE at the center is considerably smaller than that elsewhere in the shell.

The frequency dependence of the solutions for the E-and H-fields of the shell are shown in Figure 8 for a frequency range from 100 kHz to 10 MHz. As these are relatively low frequencies for the ~ 1 meter sphere size, we do not expect much of a change in the shape of the E-field distribution, but with a change in the E-field amplitude within the shell. This is confirmed by the data in these plots. Clearly, as the frequency increases, the internal field strength is reduced, due to the inductive shielding provided by the currents flowing in the shell [22].

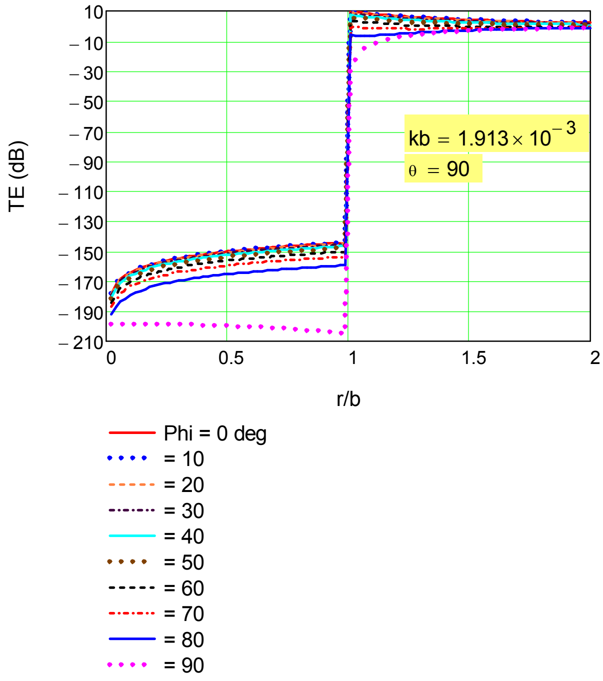

a. Electric field

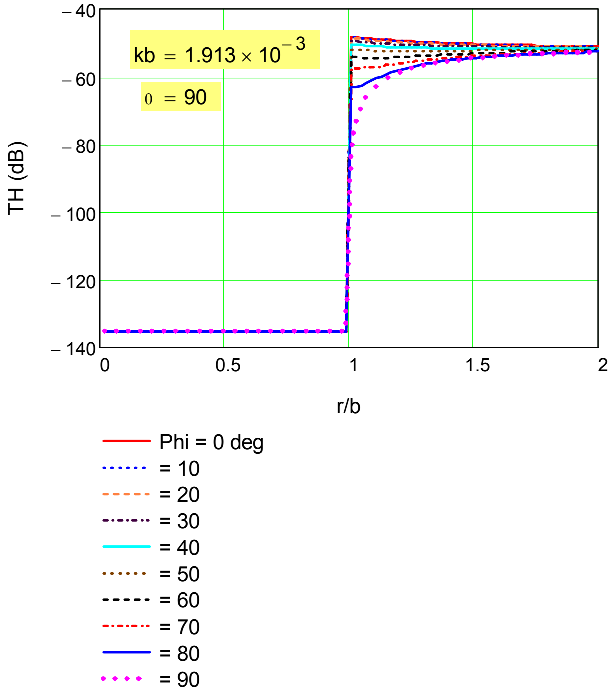

b. Magnetic field

Figure 5. Plots of the total E- and H-field transfer functions in the equatorial ($z = 0$) plane along different trajectories defined by the angle ϕ. (Parameters are $b = 0.914$ m, $\Delta = 0.794$ mm, and $f = 100$ kHz.)

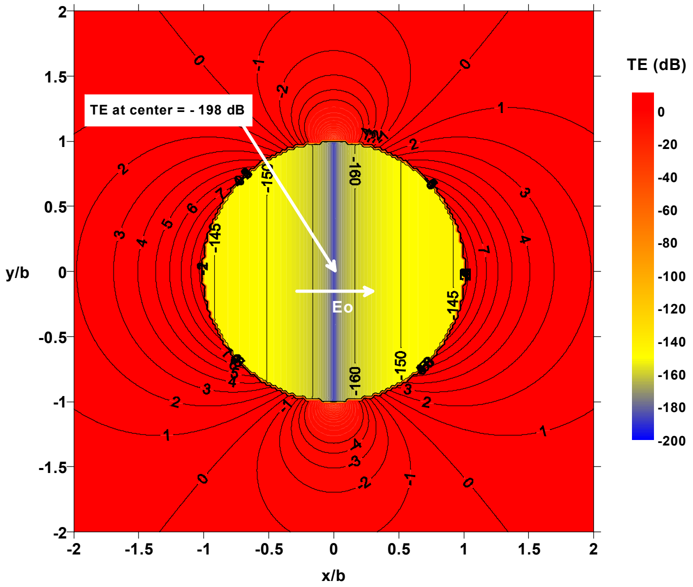

Figure 6. Contour plot of the total E-field transfer function (in dB) in the equatorial plane, inside and outside the aluminum shell, for $b = 0.914$ m, $\Delta = 0.794$ mm, and $f = 100$ kHz.

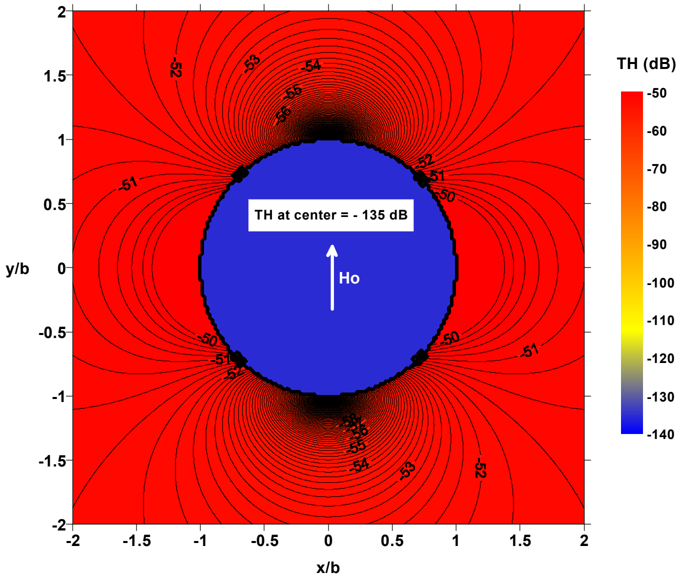

Figure 7. Contour plot of the total H-field transfer function (in dB) in the equatorial plane, inside and outside the aluminum shell, for $b = 0.914$ m, $\Delta = 0.794$ mm, and $f = 100$ kHz.

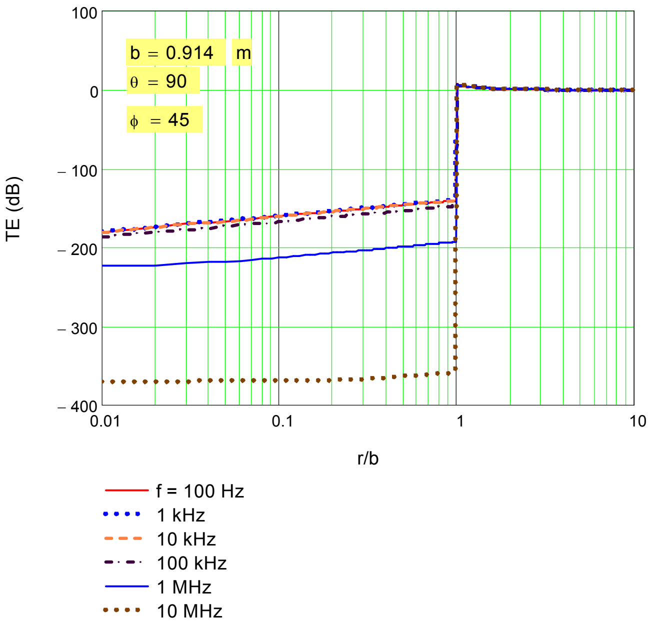

a. Electric field

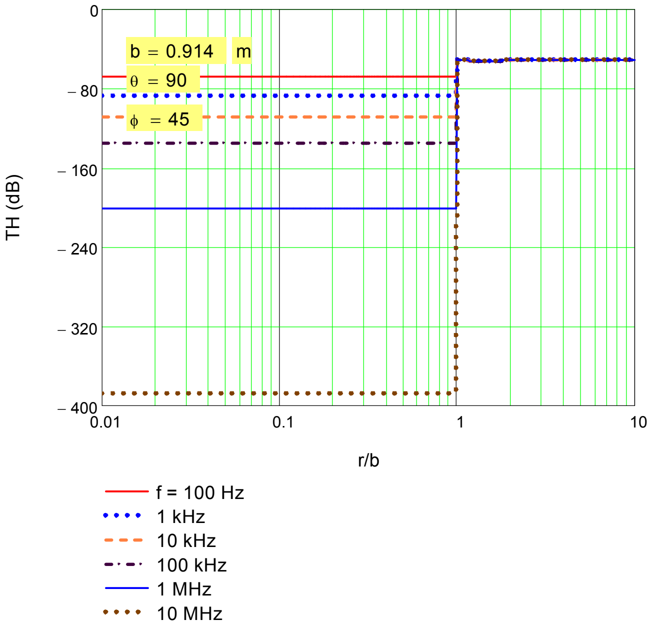

b. Magnetic field

Figure 8. Illustration of the frequency dependence of the E- and H-field transfer functions, along a radial path defined by the angles $\theta = 90^{o}$ and $\phi = 45^{o}$ for the aluminum shell with $b = 0.914$ m and $\Delta = 0.794$ mm.

F. *Statistical Description of the Internal Fields*

To get a better quantitative description of the behavior of the EM fields within the spherical shell, Monte Carlo calculations were conducted for a wide range of frequencies on the aluminum shell (b = 0.914 m and Δ = 0.794 mm). In these simulations, the total E and H-fields at about 1000 randomly selected points within the shell were calculated and the response amplitudes were binned into histograms representing probability density functions. As an example, Figure 9 presents the histograms for the E-fields, computed at a frequency of 100 MHz. Clearly the H-field is a constant within the sphere, but the E-field has a wide range of values.

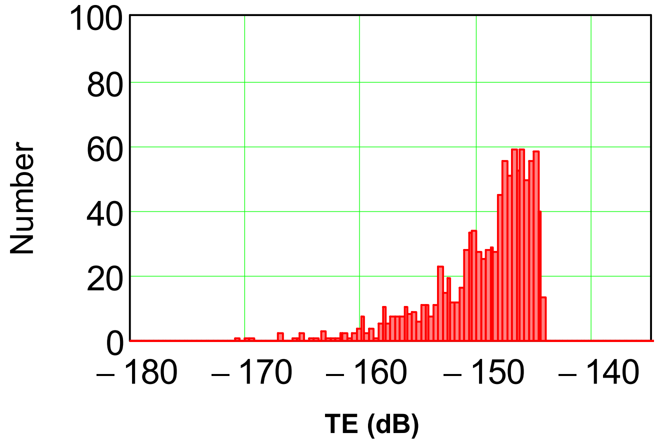

a. Electric field

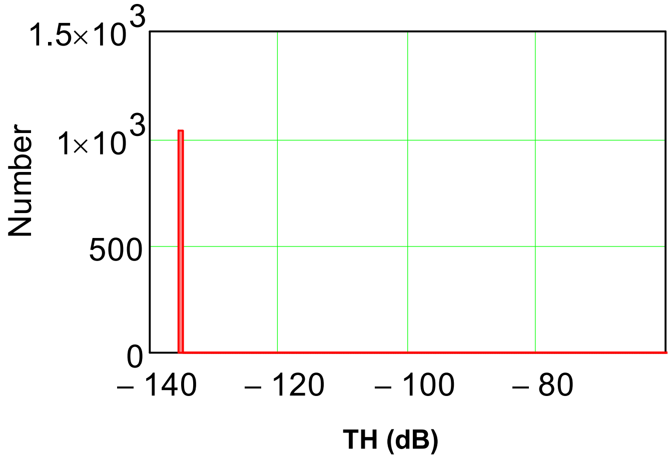

b. Magnetic field

Figure 9. Example of the histogram functions for the internal E and H-fields for the aluminum sphere, at a frequency of 100 MHz.

From the histogram distributions, cumulative probability distributions (CPDs) can be calculated. Such distributions for the E-field are shown in Figure 10. These distributions represent the probability of a randomly selected point in the shell having a TE *less than* the value specified on the *x*-axis.

As noted in this figure, at very low frequencies (from 100 Hz to 10 KHz), the E-field CPDs are virtual overlays. At higher frequencies, the shielding begins to improve and the average values of the shielding becomes larger, with slight changes in the shape of the distributions.

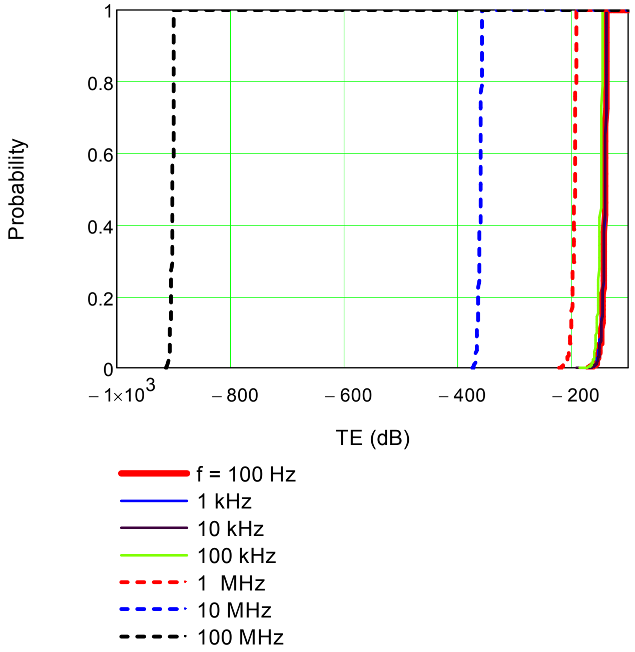

a. Complete frequency range

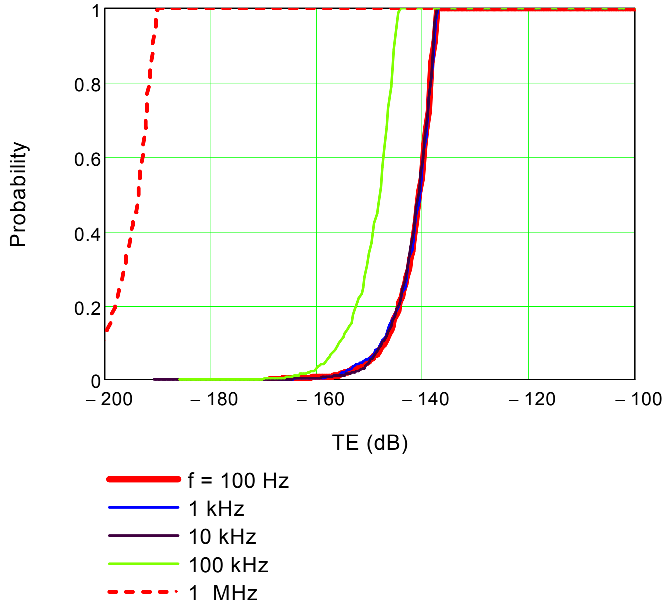

b. Low frequency range

Figure 10. Cumulative probability distributions for the E-field within the aluminum shell ($b = 0.914$ m and $\Delta = 0.794$ mm), shown for various frequencies.

As expected, the H-field CPDs are much less interesting, due to the almost uniform nature of the internal H-field in the shell. Figure 11 presents these results, where there is a slight hint of a change in the slope of the CPD at high frequencies.

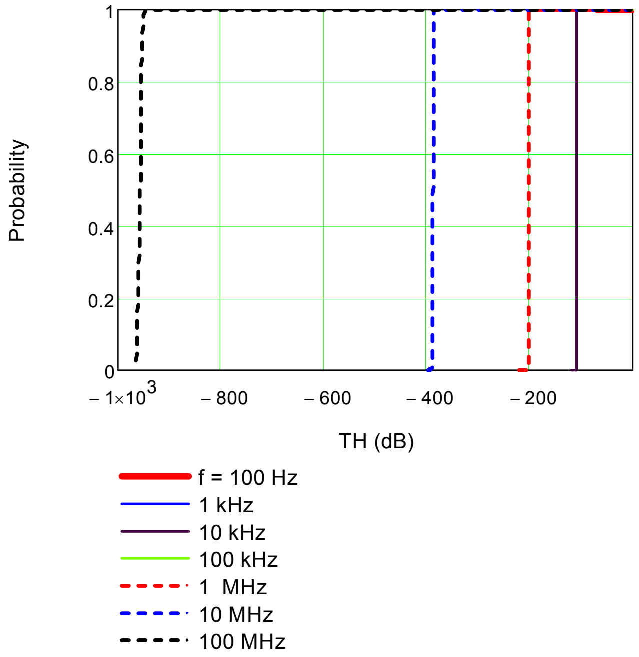

Figure 11. Cumulative probability distributions for the H-field within the aluminum shell, shown for various frequencies.

One way of summarizing the distributions of the internal field is by the mean value and standard deviation of the histograms. These quantities have been computed for the aluminum shell and are listed in Table 3. In addition to the data computed for the E-fields within the entire shell volume, the shielding values for the E-field and H-field at the center of the sphere from [8] are also listed.

From this summary, it is clear that the use of the H-field at the center of the shell as a representative sample of the shielding anywhere in the shell is a good measure. However, the same is not the case for the E-field at low frequencies, say below 1 MHz.

Table 3. Summary of the mean values and standard deviations of the distributions computed for the internal E- and H-fields of the aluminum shell.

Case	Frequency (Hz)	Avg. TE (dB)	TE Std. Dev. (dB)	TE (dB) from Ref.[8]	Avg. TH (dB)	TH Std. Dev. (dB)	TH (dB) from Ref.[8]
1	1.0E+02	-142	4.3	-251	-68	0.1	-68
2	1.0E+03	-142	4.2	-231	-88	0.1	-88
3	1.0E+04	-142	4.4	-211	-108	0.0	-108
4	1.0E+05	-149	4.4	-199	-135	0.0	-135
5	1.0E+06	-195	4.7	-224	-201	0.1	-201
6	1.0E+07	-360	3.1	-370	-388	0.4	-387
7	1.0E+08	-902	2.3	-900	-956	3.8	-958

III. LOW FREQUENCY EM SHIELDING BY A SPHERICAL SHELL WITH AN APERTURE

As mentioned earlier, a completely closed spherical shield is not the best geometry to use for trying to represent the shielding of a realistic enclosure, because most enclosures have apertures or conducting penetrations. To better understand the effect of an aperture on the shielding of a spherical enclosure, the quasi-static models of Casey [17] can be used. These models are useful for electrically small enclosures, where $k_2 b < 1$. For higher frequencies, the dynamic model of ref. [18] can be used, but this is not discussed further here.

Figure 12 shows the geometry of an infinitesimally thin, perfectly conducting spherical shell of radius b with an aperture, which is immersed in a quasi-static E-field. Two different orientations of the E-field are considered: Case 1 is with the E-field oriented in the $\hat{z}$ direction, and Case 2 is with the E-field in the $\hat{x}$ direction. The aperture is located symmetrically at the bottom of the sphere and is defined by the opening half-angle θ_o, or by the angle $\alpha = \pi - \theta_o$.

For this sphere with aperture, we are interested in computing the internal E- and H-fields and describing their statistical distributions throughout the shielded volume. In [17], both the E-field excitations and the dual H-field excitations of the sphere have been formulated. Reference [17] shows that the E- and H-field solutions for this geometry are related, with Case 1 for the E-field having the same solution as Case 2 for the H-field, and vice versa. In the development in the present paper, we will consider only the behavior of the E-field for the two cases[5].

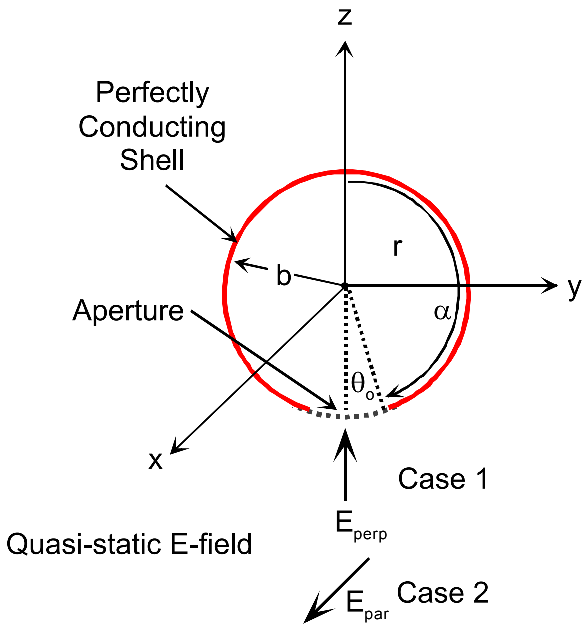

Figure 12. Geometry of a thin, perfectly conducting sphere having a circular aperture and illuminated by a quasi-static E-field.

In using this quasi-static shielding model it is important to keep in mind that it is inherently different from the penetrable spherical shield model discusses in Section 2, where at low frequencies the H-field is able to diffuse easily into the shield. In the present model with an assumed perfectly conducting shield, this diffusion mechanism is not present and the shield does provide shielding of the H-field.

A. Case 1 -- Axially Symmetric Excitation of the Uncharged Sphere with Aperture

For the case of the z-directed excitation E-field, the solution is independent of the ϕ coordinate. From quasi-static considerations, the electric potential function for this “incident” E-field is

---

[5] This is not to underemphasize the need for knowing the internal H-field, however. As noted in ref.[23], the excitation of an internal wire in the sphere with an aperture requires knowledge of both the E- and H-fields.

$$V^i(r,\theta) = -E_o r\cos\theta \tag{31}$$

and the potential function arising from induced charges on the sphere with hole can be expressed as a sum of static functions as

$$\begin{aligned} V^s(r,\theta) &= E_o b\sum_{n=0}^{\infty} a_n^{(1)}\left(\frac{r}{b}\right)^{n} P_n\left(\cos\theta\right) \quad (r\le b) \\ &= E_o b\sum_{n=0}^{\infty} a_n^{(1)}\left(\frac{r}{b}\right)^{-(n+1)} P_n\left(\cos\theta\right) \quad (r\ge b) \end{aligned} \tag{32}$$

where $P_n\left(\cos\theta\right)$ is the Legendre polynomial of order *n*, and $a_n^{(1)}$ are unknown expansion coefficients. The total potential is the sum of the two:

$$V(r,\theta) = V^i(r,\theta) + V^s(r,\theta)\,. \tag{33}$$

By using boundary conditions on the sphere that $V(b,\theta) = V_o$ a constant (but unknown) for $0 \le \theta < \alpha$ and that $\partial V(r,\theta)/\partial r$ is continuous over the opening ($r = b$, $\alpha < \theta \le \pi$), Casey shows that by using Eqs.(31) and (32) the boundary conditions can be put into a dual series equation of the form

$$\begin{aligned} &\sum_{n=0}^{\infty} a_n^{(1)} P_n\left(\cos\theta\right) = \frac{V_o}{E_o b} + \cos\theta \qquad (0\le\theta<\alpha) \\ &\sum_{n=0}^{\infty} (2n+1) a_n^{(1)} P_n\left(\cos\theta\right) = 0 \qquad (\alpha<\theta\le\pi) \end{aligned} \tag{34}$$

Using the assumption that the sphere is uncharged, Casey further notes that the $n = 0$ term in the series must vanish and he then develops an analytical solution for the coefficients $a_n^{(1)}$. (See [17] for more details). The resulting solution is

$$\begin{aligned} a_n^{(1)} = &\frac{1}{\pi}\left(\frac{\sin(n-1)\alpha}{n-1} + \frac{\sin(n+2)\alpha}{n+2}\right) - \\ &\frac{1}{\pi}\left(\frac{\sin\alpha + \frac{1}{2}\sin 2\alpha}{\alpha + \sin\alpha}\right)\left(\frac{\sin n\alpha}{n} + \frac{\sin(n+1)\alpha}{n+1}\right) \end{aligned}. \tag{35}$$

The E-field is computed from the total potential as

$$\begin{aligned} E\left(r,\theta,\phi\right) &= -\nabla V\left(r,\theta,\phi\right) \\ &= \frac{\partial V}{\partial r}\hat{r} + \frac{1}{r}\frac{\partial V}{\partial\theta}\hat{\theta} + \frac{1}{r\sin\theta}\frac{\partial V}{\partial\phi}\hat{\phi} \end{aligned}, \tag{36}$$

or in component form,

$$\begin{aligned} E_r(r,\theta) &= E_o\cos\theta - \\ &\quad E_o\sum_{n=1}^{\infty} a_n^{(1)} n\left(\frac{r}{b}\right)^{n-1} P_n(\cos\theta) \qquad (\text{for } r<b) \\ &= E_o\cos\theta + \\ &\quad E_o\sum_{n=1}^{\infty} a_n^{(1)}(n+1)\left(\frac{r}{b}\right)^{-(n+2)} P_n(\cos\theta) \quad (\text{for } r>b) \end{aligned} \tag{37a}$$

$$\begin{aligned} E_\theta(r,\theta) &= -E_o\sin\theta - \\ &\quad E_o\sum_{n=1}^{\infty} a_n^{(1)}\left(\frac{r}{b}\right)^{n-1} P_n^1(\cos\theta) \qquad (\text{for } r<b) \\ &= -E_o\sin\theta - \\ &\quad E_o\sum_{n=1}^{\infty} a_n^{(1)}\left(\frac{r}{b}\right)^{-(n+2)} P_n^1(\cos\theta) \quad (\text{for } r>b) \end{aligned} \tag{37b}$$

$$E_\phi(r,\theta) = 0\,\cdot \tag{37c}$$

In Eq.(37b) the relationship

$$\frac{dP_n(\cos\theta)}{d\theta} = P_n^1(\cos\theta) \tag{38}$$

is used.

Casey computes the E-field at the center of the sphere, where only the n = 1 term contributes to the sum. In this case, he gets an E-field transfer function in closed form as

$$\begin{aligned} TE^{(1)} &\equiv \frac{\left|E^{in}(0)\right|}{E_o} \\ &= \frac{1}{\pi}\left[\theta_o - \frac{1}{3}\sin 3\theta_o + \frac{\left(\sin\theta_o - \frac{1}{2}\sin 2\theta_o\right)}{\pi - \theta_o + \sin\theta_o}\right] \end{aligned} \tag{39}$$

where $\theta_o = \pi - \alpha$ is the opening angle of the aperture in the sphere shown in Figure 12.

B. Case 2 – X-directed E-field Excitation of the Uncharged Sphere with Aperture

The potential function for excitation field in x- direction is

$$V^i(r,\theta) = -E_o r\sin\theta\cos\phi \tag{40}$$

and the corresponding potential arising from interaction with the sphere with hole is

$$\begin{aligned} V^s(r,\theta,\phi) &= E_o b\cos\phi\sum_{n=0}^{\infty} a_n^{(2)}\left(\frac{r}{b}\right)^{n} P_n^1\left(\cos\theta\right) \qquad (r\le b) \\ &= E_o b\cos\phi\sum_{n=0}^{\infty} a_n^{(2)}\left(\frac{r}{b}\right)^{-(n+1)} P_n^1\left(\cos\theta\right) \quad (r\ge b) \end{aligned}. \tag{41}$$

In this expression, the associated Legendre polynomials $P_n^1\left(\cos\theta\right)$ are used and the expansion coefficients $a_n^{(2)}$ are different from those found for Case 1. Noting that symmetry in this case requires that the total potential on the sphere be zero and applying the previously mentioned boundary conditions, Casey develops another dual series equation for the unknown coefficients for this case:

$$\begin{aligned} &\sum_{n=0}^{\infty} a_n^{(2)} P_n^1\left(\cos\theta\right) = \sin\theta \qquad (0\le\theta<\alpha) \\ &\sum_{n=0}^{\infty} (2n+1) a_n^{(2)} P_n^1\left(\cos\theta\right) = 0 \qquad (\alpha<\theta\le\pi) \end{aligned}. \tag{42}$$

with the solution for $a_n^{(2)}$ being

$$a_n^{(2)} = \frac{-1}{\pi n(n+1)} \left(\begin{array}{l} \frac{n+1}{n-1}\sin(n-1)\alpha + \sin n\alpha - \\ \sin(n+1)\alpha - \frac{n}{n+2}\sin(n+2)\alpha \end{array} \right) \tag{43}$$

The resulting E-field components inside and outside the sphere are calculated from Eq.(36) as

$$\begin{aligned} E_r(r,\theta,\phi) &= E_o \sin\theta\cos\phi - \\ &\quad E_o \cos\phi \sum_{n=1}^{\infty} a_n^{(2)} n \left(\frac{r}{b}\right)^{n-1} P_n^1(\cos\theta) \qquad (\text{for } r<b) \\ &= E_o \,\text{in}\,\theta\cos\phi + \\ &\quad E_o \cos\phi \sum_{n=1}^{\infty} a_n^{(2)} (n+1) \left(\frac{r}{b}\right)^{-(n+2)} P_n^1(\cos\theta) \quad (\text{for } r>b) \end{aligned} \tag{44a}$$

$$\begin{aligned} E_\theta(r,\theta,\phi) &= E_o \cos\theta\cos\phi - \\ &\quad E_o \cos\phi \sum_{n=1}^{\infty} a_n^{(2)} \left(\frac{r}{b}\right)^{n-1} \frac{\partial}{\partial\theta} P_n^1(\cos\theta) \qquad (\text{for } r<b) \\ &= E_o \cos\theta\cos\phi - \\ &\quad E_o \cos\phi \sum_{n=1}^{\infty} a_n^{(2)} \left(\frac{r}{b}\right)^{-(n+2)} \frac{\partial}{\partial\theta} P_n^1(\cos\theta) \quad (\text{for } r>b) \end{aligned} \tag{44b}$$

$$\begin{aligned} E_\phi(r,\theta,\phi) &= -E_o \sin\phi + \\ &\quad E_o \frac{\sin\phi}{\sin\theta} \sum_{n=1}^{\infty} a_n^{(2)} \left(\frac{r}{b}\right)^{n-1} P_n^1(\cos\theta) \qquad (\text{for } r<b) \\ &= -E_o \sin\phi + \\ &\quad E_o \frac{\sin\phi}{\sin\theta} \sum_{n=1}^{\infty} a_n^{(2)} \left(\frac{r}{b}\right)^{-(n+2)} P_n^1(\cos\theta) \quad (\text{for } r>b) \\ &\quad . \end{aligned} \tag{44c}$$

In Eq.(44b) the derivative of the associated Legendre function can be calculated from the relationship

$$\frac{\partial}{\partial\theta} P_n^m(\cos\theta) = \frac{-1}{\sin\theta} \left[\begin{array}{l} (n+1)\cos\theta\, P_n^m(\cos) - \\ (n-m+1) P_{n+1}^m(\cos\theta) \end{array} \right] \tag{45}$$

For this excitation, the E-field transfer function at the center of the sphere given by Casey as

$$TE^{(2)} = \frac{1}{\pi}\left[\theta_o - \frac{1}{2}\sin\theta_o - \frac{1}{2}\sin 2\theta_o + \frac{1}{6}\sin 3\theta_o \right]. \tag{46}$$

C. *Numerical Results*

The $\hat{r}$, $\hat{\theta}$ and $\hat{\phi}$ components E-fields in the vicinity of the sphere given by Eqs.(37) and (44) have been calculated numerically and a total E-field transfer function TE developed as in Eq.(30). As in ref. [18], it was found that a large number of terms in the summations were required to achieve convergence throughout the sphere. Typically, 150 terms were used for the present calculations.

Figure 13 presents a comparison of the calculated TE functions at the center of the sphere for Case 1 and Case 2 with those reported by ref. [17] (in Casey's Figure 2). This plot depicts the variation of the shielding as the aperture half-angle θ_O varies from zero (no aperture) to 180° (no sphere).

The present analysis overlays exactly on Casey's results, and partially validates the numerical implementation of the solution. Figure 14 presents the same shielding data as in Figure 13, but with TE expressed in dB.

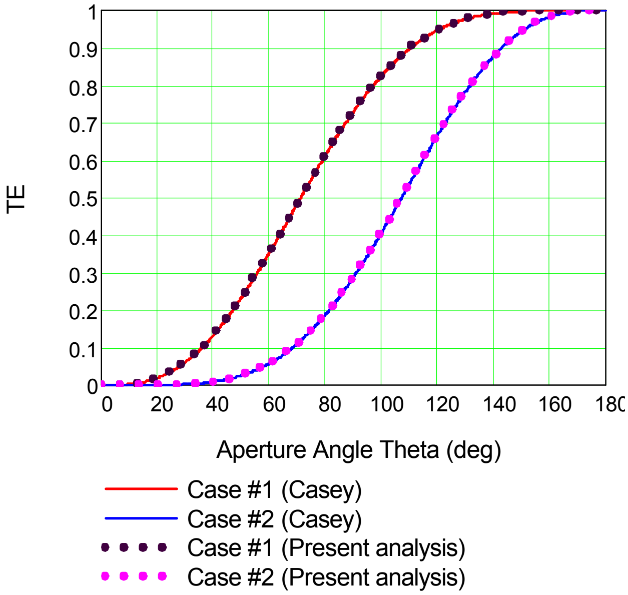

Figure 13. Plot of the E-field transfer function at the center of the spherical enclosure as a function of the aperture half-angle θ_O, for Case 1 (E in z-direction) and Case 2 (E in x-direction).

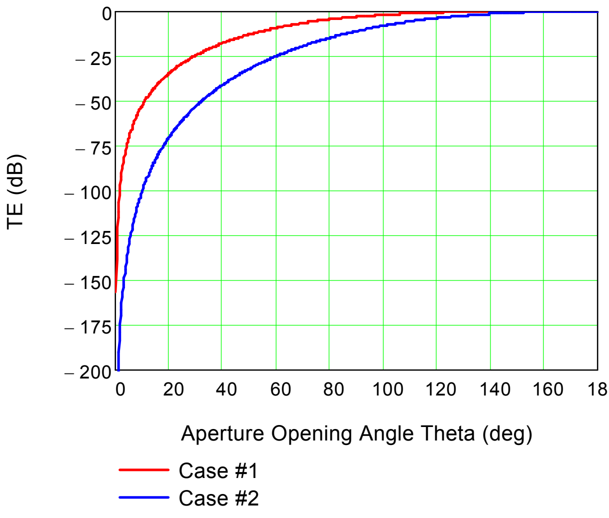

Figure 14. Plots of the E-field transfer function (expressed in dB) at the center of the sphere, as a function of the aperture angle θ_O.

Since Eqs.(37) and (44) are valid inside and outside the sphere, it is possible to develop contour plots of the total E-field transfer functions that show the E-field leaking into the sphere through the aperture. Figure 15 shows contours of TE (in dB) in the vertical z-x plane for the two different excitation E-field directions. For these particular plots, the aperture half-angle is $\theta_O = 10°$.

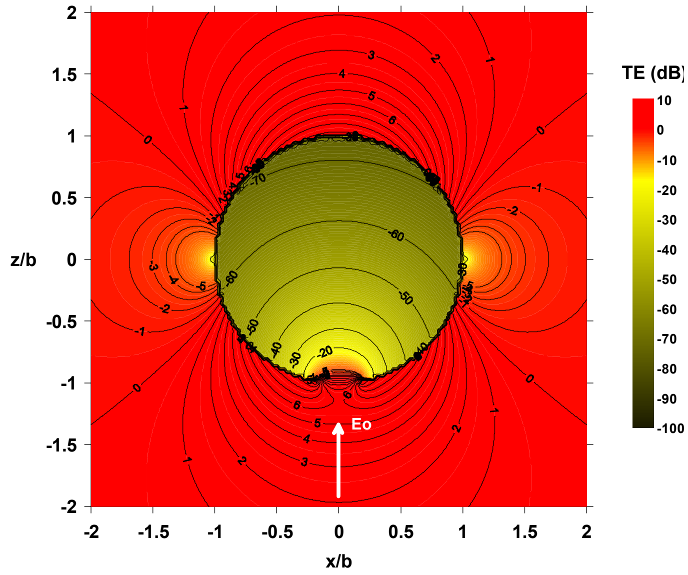

a. Case #1 (*E* in z-direction)

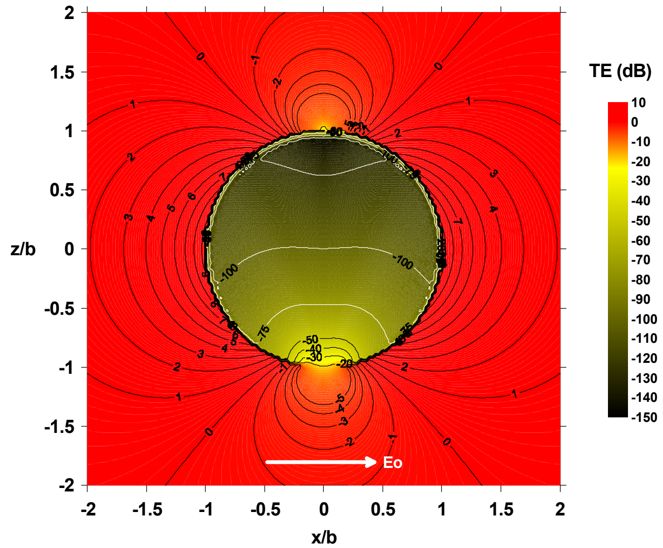

b. Case #2 (*E* in x-direction)

Figure 15. Contour plots of TE (in dB) in the vertical *z-x* plane for Case 1 (*a*) and Case 2 (*b*) excitations. (Aperture half-angle $\theta_O = 10^O$).

D. *Statistical Description of the Internal Fields*

A Monte Carlo simulation with 3000 random internal points was conducted and the results for the total E-fields for Cases 1 and 2 binned. For the aperture half-angle of $\theta_O = 10^O$, Figure 16 shows the resulting histograms, which are typical of those for the other angles.

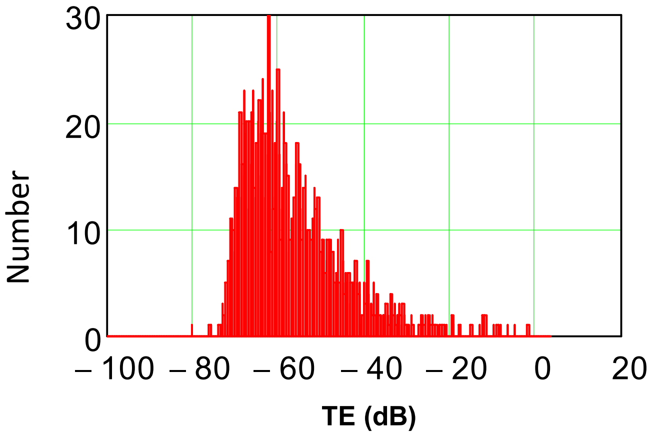

a. Case #1 (*E* in *z*-direction)

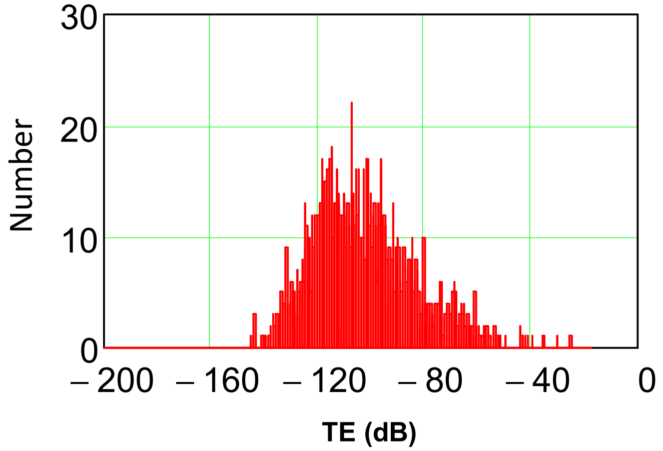

b. Case #2 (E in x-direction)

Figure 16. Example of the histogram functions for the internal E-field transfer functions for an aperture half-angle of $\theta_O = 10^O$.

Calculations were performed for aperture half-angles of 1, 2, 5, 10, 20, 30, 45 and 90 degrees and the CPDs of the E-field transfer functions computed. Figure 17 presents the results for Case 1 and the Case 2 results are in Figure 18. Also shown in these figures is a close-up plot of the responses near 0 dB, which show that there are some points within the $r = b$ sphere that have E-fields larger than the excitation field. This occurs at points near the rim of the aperture, where the E-field is large due to the sharp edge.

Table 4 summarizes these distributions by the mean values of the E-field transfer function and the standard deviations. Also shown is the TE value at the center of the sphere. While this value is not exactly equal to the mean value of TE, it is usually within about 5 dB of the mean. Thus, the value at the center does provide a useful measure of the average shielding provided by this structure.

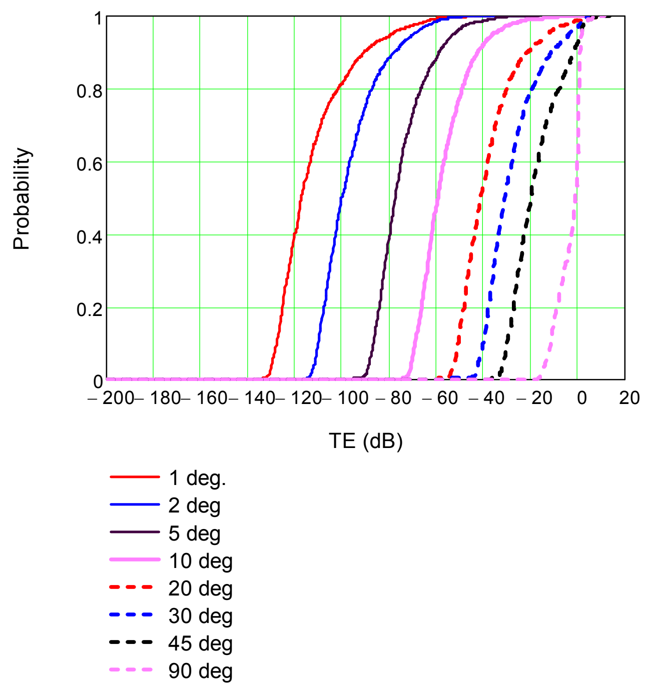

a. All responses

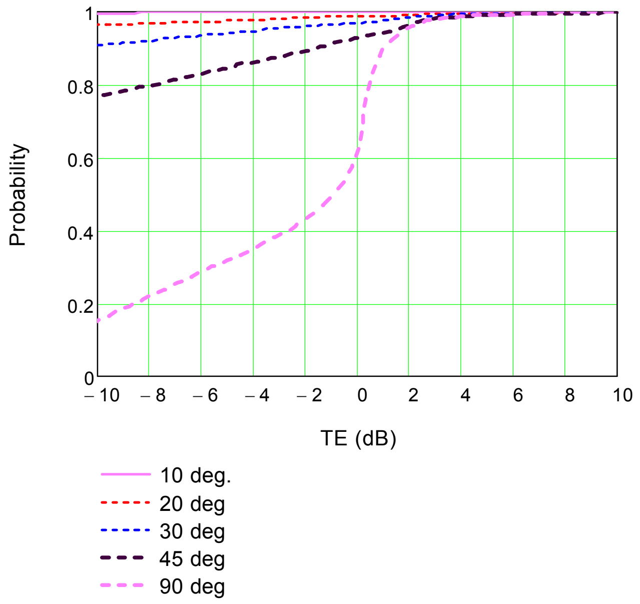

b. Expanded scale near 0 dB

Figure 17. Cumulative probability distributions for the E-field within the sphere with aperture for Case 1, shown for various values of the aperture half-angle θ_o.

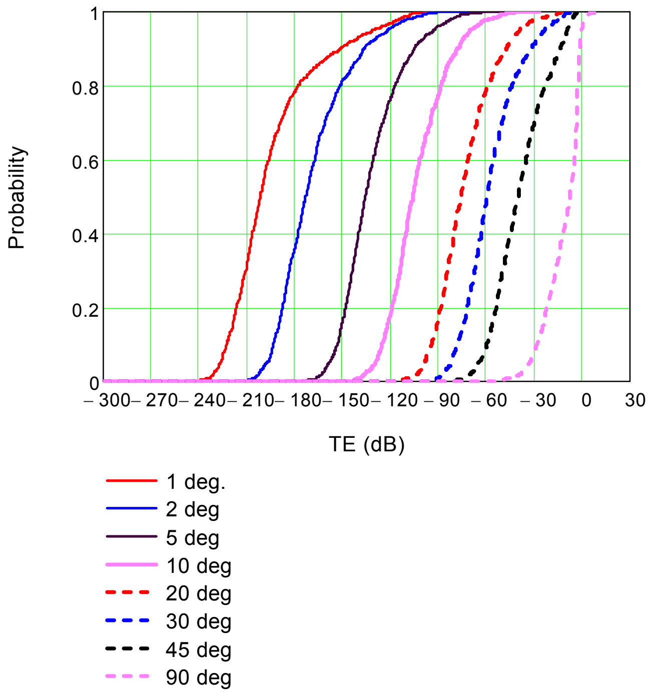

a. All responses

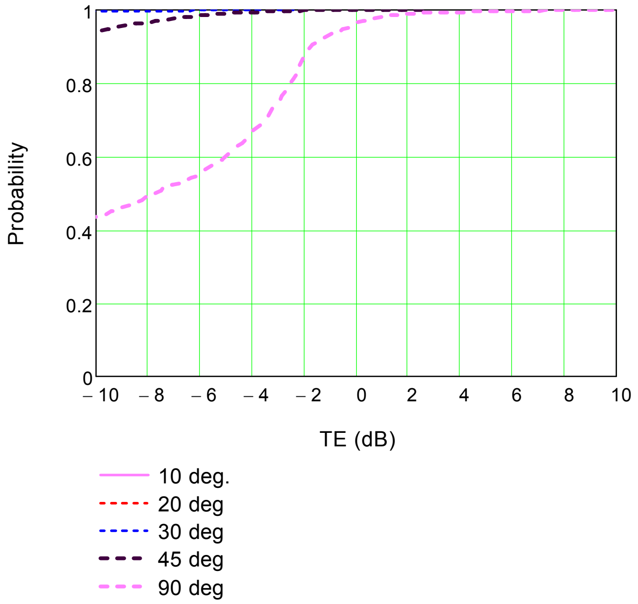

b. Expanded scale near 0 dB

Figure 18. Cumulative probability distributions for the E-field within the sphere with aperture for Case 2, shown for various values of the aperture half-angle θ_o.

Table 3. Summary of the mean values and standard deviations of the distributions computed for the internal E-fields in the sphere with aperture.

	Case 1			Case 2		
Aperture Angle (deg)	Avg. TE (dB)	TE Std. Dev. (dB)	TE (dB) from [17]	Avg. TE (dB)	TE Std. Dev. (dB)	TE (dB) from [17]
1	-112.6	15.6	-111.9	-194.3	28.1	-199.7
2	-96.7	12.9	-93.9	-168.4	22.8	-169.6
5	-74.8	11.3	-70.0	-131.9	19.5	-129.9
10	-57.0	11.1	-52.0	-103.4	18.5	-99.8
20	-38.2	12.1	-34.3	-73.1	18.2	-69.9
30	-28.0	11.4	-24.3	-57.1	17.4	-52.7
45	-17.8	10.2	-14.9	-38.7	16.9	-36.0
90	-3.2	5.1	-2.7	-11.6	11.0	-10.8

IV. SUMMARY AND COMMENTS

This paper has examined two canonical shielding problems with the goal of gaining a better understanding of the EM shielding provided by real shielding enclosures. The shield considered here was a spherical shell – one being made of finitely conducting material (aluminum) and having a finite wall thickness, and the second being a very thin, perfectly conducting hollow sphere with an aperture. In the study described in this paper, the analysis for the first case was frequency-dependent, while the analysis for the second was quasi-static.

The reason for choosing these simple shapes was that the calculation of the internal fields could be done mathematically through the use of spherical harmonics. This provides the possibility of evaluating the E- and H-fields anywhere inside or outside the sphere. In this analysis, closed form expressions for the expansion coefficients were found and these do not appear to be generally available in the literature. Moreover, a scaling technique was introduced that permits the accurate evaluation of the spherical Hankel function terms of the wave functions. This scaling is not an approximation to the Hankel functions as obtained by [11] and others, but is exact.

The benefit of this type of solution is that a Monte Carlo simulation can be used to develop probability distributions for the internal fields, which show the variability of the field magnitudes inside the sphere. The difficulty, however, is that the solution is in the form of an infinite series of factors, which, at times, is difficult to sum. Moreover, there are numerical challenges in calculating the required Hankel functions of complex argument inside the lossy material due to numerical overflow and underflow.

From the formulation and application of the model described in this paper, the following observations regarding the shielding of the sphere deserve mention:

1. Most previous shielding studies of spherical shapes have concentrated on the behavior of the E- and H-fields at the center of the sphere. For a uniform sphere made of finitely conducting material, the use of the center as an observation point is appropriate for the H-field, as this internal field is seen to be nearly constant. However, it is not appropriate for the E-field, since there can be large variations of this field inside the sphere and the E-field at the center is very low. This provides a gross overestimate of the amount of E-field shielding provided by the sphere.
2. A better way to describe the internal fields within the sphere (and any other enclosure, for that matter) is through a cumulative probability distribution that represents that variation of the internal fields
3. For the perfectly conducting spherical shell with an aperture, there are also large variations of the E- and H-fields within the interior. However, it is noted that for this type of shield, the value of the field at the center of the sphere is close to the average value of the field inside – at least for apertures with opening half-angles from 0 to 90 degrees. Nevertheless, there can be significant variations of the internal fields, with a standard deviation of 5 to 30 dB being noted the cases considered here.
4. Finally, while not considered here, but very important nevertheless, the presence of conducting

penetrations into the interior of the sphere will radically change the statistical behavior of the internal fields. Since this type of penetration is very common, the shielding of most practical enclosures will be ultimately determined by this type of penetration and not by diffusion and aperture penetrations that have been considered in this paper. Clearly this area requires more investigation and quantification.

V. REFERENCES

[1] "IEEE Standard Method for Measuring the Effectiveness of Electromagnetic Shielding Enclosures", IEEE STD 299-1997, 9 December 1997.

[2] "High-Altitude Electromagnetic Pulse (HEMP) Protection for Ground-Based C4I Facilities Performing Critical, Time-Urgent Missions", MIL-STD-188-125-1, 17 July 1998.

[3] IEC-61000-5-6, Electromagnetic Compatibility, Part 5: Mitigation Methods and Installation Guidelines, Section 6: Mitigation of External Influences, 2002-06.

[4] Lee, K. S. H., ed., EMP Interaction: Principles, Techniques and Reference Data, Hemisphere Publishing Co. New York, 1989.

[5] Lee, K. S. H., and G. Bedrosian, "Diffusive Electromagnetic Penetration into Metallic Enclosures", IEEE Trans AP, Vol. AP-27, No. 2, March 1979.

[6] Kunz, K. S. and R. J. Luebbers, The Finite Difference Time Domain Method for Electromagnetics, CRC Press, Boca Raton, FL, 1993.

[7] Stratton, J. A., Electromagnetic Theory, McGraw-Hill Book Co., New York, 1941.

[8] Harrison, C. W. and C. H. Papas, "On the Attenuation of Transient Fields by Imperfectly Conducting Spherical Shells", IEEE Trans AP, Vol. AP-18, No 6, Nov. 1965.

[9] Lindell, I. V., "Minimum Attenuation of Spherical Shields", IEEE Trans AP, Vol. AP-16, pp. 369-371, May 1968.

[10] Shastry, S. V. K., K. N. Shamanna, and V. R. Katti, "Shielding of Electromagnetic Fields of Current Sources by Hemispherical Enclosures", IEEE Trans AP, Vol. EMC-27, No. 4, November 1985.

[11] Baum C. E., "The Boundary-Connection Supermatrix for Uniform Isotropic Walls", Interaction Notes, Note 562, Air Force Research laboratory Directed Energy Directorate, 22 October 2000.

[12] Franceschetti, G., "Fundamentals of Steady State and Transient Electromagnetic Fields in Shielding Enclosures," IEEE Trans. EMC, Vol. EMC-21, 1979.

[13] Chang, S., "Scattering by a Spherical Shell with a Circular Aperture", University of Michigan technical report 5548-T-RL-2069, January 1968.

[14] Ziolkowski, R. D. P. Marsland. L. F. Libelo and G.E. Pisane, "Scattering from an Open Spherical Shell Having a Circular Aperture and Enclosing a Concentric Dielectric Sphere", IEEE Trans AP., Vol. 36, No. 7, July 1988.

[15] Enander, B., "Scattering by a Spherical Shell With a Small Circular Aperture", EMP Interaction Notes, Note 77, August 1971.

[16] Sancer, M. I, and N. A. Varvatsis, "Electromagnetic Penetrability of Perfectly Conducting Bodies Containing an Aperture", EMP Interaction Notes, Note 49, August 1970.

[17] Casey, K. F., "Quasi-Static Electric- and Magnetic-Field Penetration of a Spherical Shield Through a Circular Aperture", IEEE Trans EMC, Vol. EMC-27, No. 1, February 1985.

[18] Senior, T. B. A., and G. Desjardins, "Electromagnetic Field Penetration into a Spherical Cavity", IEEE Trans EMC, Vol. EMC-16, No. 4, November 1974.

[19] Abramowitz, M. and I. A. Stegun, Handbook of Mathematical Functions, U.S. National Bureau of Standards, Washington, DC 1964.

[20] Personal conversation with Prof. Chalmers Butler, ECE Department, Clemson University, May 2008.

[21] Harrington, R. F., Time Harmonic Electromagnetic Fields, McGraw-Hill Book Co., New York, 1961.

[22] Hoburg, J. F., "Principles of Quasi-static Magnetic Shielding with Cylindrical and Spherical Shields", IEEE Trans. EMC, Vol. 37, No. 4, November 1995.

[23] Yang, F. C. and C. E. Baum, "Use of Matrix Norms of Interaction Supermatrix Blocks for Specifying Electromagnetic Performance of Subshields", Interaction Notes, Note 427, April 1983.

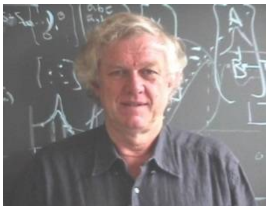

Frederick M. Tesche (S'68–M'71–SM'78–F'92 –LF'10) received the B.S. and Ph.D. degrees from the University of California, Berkeley, in 1965 and 1971, respectively, both in electrical engineering.

Up until his retirement in 2012, Dr. Tesche served as an independent consultant providing services to several firms, including Pro-Tech, SAIC, Metatech Inc., Amperion, Inc., DelCross, SRI International and Promethean Devices. Prior to forming his consulting practice in 1990, he was associated with a number of different firms, including LuTech, Inc. (a firm he co-founded in 1978 with T. K. Liu and D. V. Giri). In addition, he has served as a Research Professor at Clemson University where he conducted research into the effects of EM fields on electrical systems and networks, and developed a course on electromagnetic compatibility (EMC).